Limnol. Oceanogr., 48(2), 2003, 895–919

High-frequency internal waves in large stratified lakes

L. Boegman,[1] *J. Imberger, G. N. Ivey, and J. P. Antenucci*

Centre for Water Research, Department of Environmental Engineering, University of Western Australia, Crawley, Western Australia 6009, Australia

Abstract

Observations are presented from Lake Biwa and Lake Kinneret showing the ubiquitous and often periodic nature of high-frequency internal waves in large stratified lakes. In both lakes, high-frequency wave events were observed within two distinct categories: (1) Vertical mode 1 solitary waves near a steepened Kelvin wave front and vertical mode 2 solitary waves at the head of an intrusive thermocline jet were found to have wavelengths ~64–670 m and ~13–65 m, respectively, and were observed to excite a spectral energy peak near 10^{-3} Hz. (2) Sinusoidal vertical mode 1 waves on the crests of Kelvin waves (vertically coherent in both phase and frequency) and bordering the thermocline jets in the high shear region trailing the vertical mode 2 solitary waves (vertically incoherent in both phase and frequency) were found to have wavelengths between 28–37 and 9–35 m, respectively, and excited a spectral energy peak just below the local maximum buoyancy frequency near 10^{-2} Hz. The waves in wave event categories 1 and 2 were reasonably described by nonlinear wave and linear stability models, respectively. Analysis of the energetics of these waves suggests that the waves associated with shear instability will dissipate their energy rapidly within the lake interior and are thus responsible for patchy turbulent events that have been observed within the metalimnion. Conversely, the finite-amplitude solitary waves, which each contain as much as 1% of the basin-scale Kelvin wave energy, will propagate to the lake perimeter where they can shoal, thus contributing to the maintenance of the benthic boundary layer.

The degree of ambient stratification in lakes is significant in regulating the vertical transport of nutrients, plankton, and oxygen. Accordingly, stratification can instigate the occurrence of hypolimnetic anoxia (e.g., Mortimer 1987). Simple energy models (Imberger 1998) and microstructure (e.g., Wüest et al. 2000; Saggio and Imberger 2001) and tracer (e.g., Goudsmit et al. 1997) observations suggest that turbulent buoyancy flux, which erodes the ambient stratification, is negligible within the lake interior and occurs primarily at rates an order of magnitude greater than in the interior along the lake boundaries. The physical processes responsible for this spatial heterogeneity of mixing within the lacustrine environment are also believed to occur within larger scale oceanic flows. Observed vertical mixing rates within the vast ocean interior (e.g., Ledwell et al. 1993) are an order of magnitude smaller than classical global estimates (Munk 1966; Gregg 1987). Observations show this difference is accounted for by enhanced mixing within topographic boundary layers (e.g., Polzin et al. 1997; Ledwell et al. 2000). Our present knowledge suggests that the augmented mixing and dissipation within the lacustrine benthic boundary layer results from shear-driven turbulence as baroclinic currents oscillate along the lake bed and from the breaking of high-frequency internal waves as they shoal upon sloping boundaries at the depth of the metalimnion (Imberger 1998; Michallet and Ivey 1999; Gloor et al. 2000; Horn et al. 2001). Interior mixing is believed to result from both shear and convective instability (Saggio and Imberger 2001).

Observational records have shown high-frequency internal waves to be ubiquitous to lakes and oceans (cf. Garrett and Munk 1975). Furthermore, high-resolution sampling (e.g., Saggio and Imberger 1998; Antenucci and Imberger 2001) has provided evidence that these high-frequency internal waves exist in narrow but discrete frequency bands approaching the buoyancy frequency, N. Here $N^2 = -(g/\rho_o)(\partial\rho/\partial z)$ where $\rho(z)$ is the ambient density profile and ρ_o is a reference density. Both the narrowness of the observed frequency band and the existence of similar observations from a variety of lakes suggest common generation mechanisms. Several such mechanisms have been proposed: (1) shear instability (e.g., Woods 1968; Thorpe 1978; Sun et al. 1998; Antenucci and Imberger 2001), (2) nonlinear steepening of basin-scale internal waves (e.g., Hunkins and Fliegel 1973; Farmer 1978; Mortimer and Horn 1982; Horn et al. 2001), (3) internal hydraulic jumps (e.g., Apel et al. 1985; Holloway 1987; Farmer and Armi 1999), (4) excitation by intrusions and gravity currents (e.g., Hamblin 1977; Maxworthy et al. 1998), and (5) flow interaction with boundaries (e.g., Thorpe et al. 1996; Thorpe 1998). In this paper, the waves generated by these mechanisms are grouped into two fundamental classes: waves described by linear stability models (e.g., Kelvin–Helmholtz and Holmboe modes) and waves described by weakly nonlinear models (e.g., solitary waves).

In the following sections, we analyze observations of high-frequency internal waves from the interior of two large stratified lakes. The primary objectives are to (1) identify the occurrence of mechanisms that can lead to the excitation of

[1] Corresponding author (boegman@cwr.uwa.edu.au).

Acknowledgments

The authors acknowledge Andy Hogg and Kraig Winters for the numerical code used in the linear stability analysis and Angelo Saggio for numerous data processing scripts. We also thank Andy Hogg for providing valuable discussion on linear stability and two anonymous reviewers whose constructive suggestions improved this paper. The field work was undertaken by the Centre for Environmental Fluid Dynamics, the Lake Biwa Research Institute and the Yigal Allon Kinneret Limnological Laboratory. L.B. acknowledges the support of an International Postgraduate Research Scholarship and a University Postgraduate Award. This paper forms Centre for Water Research reference ED 1561-LB.

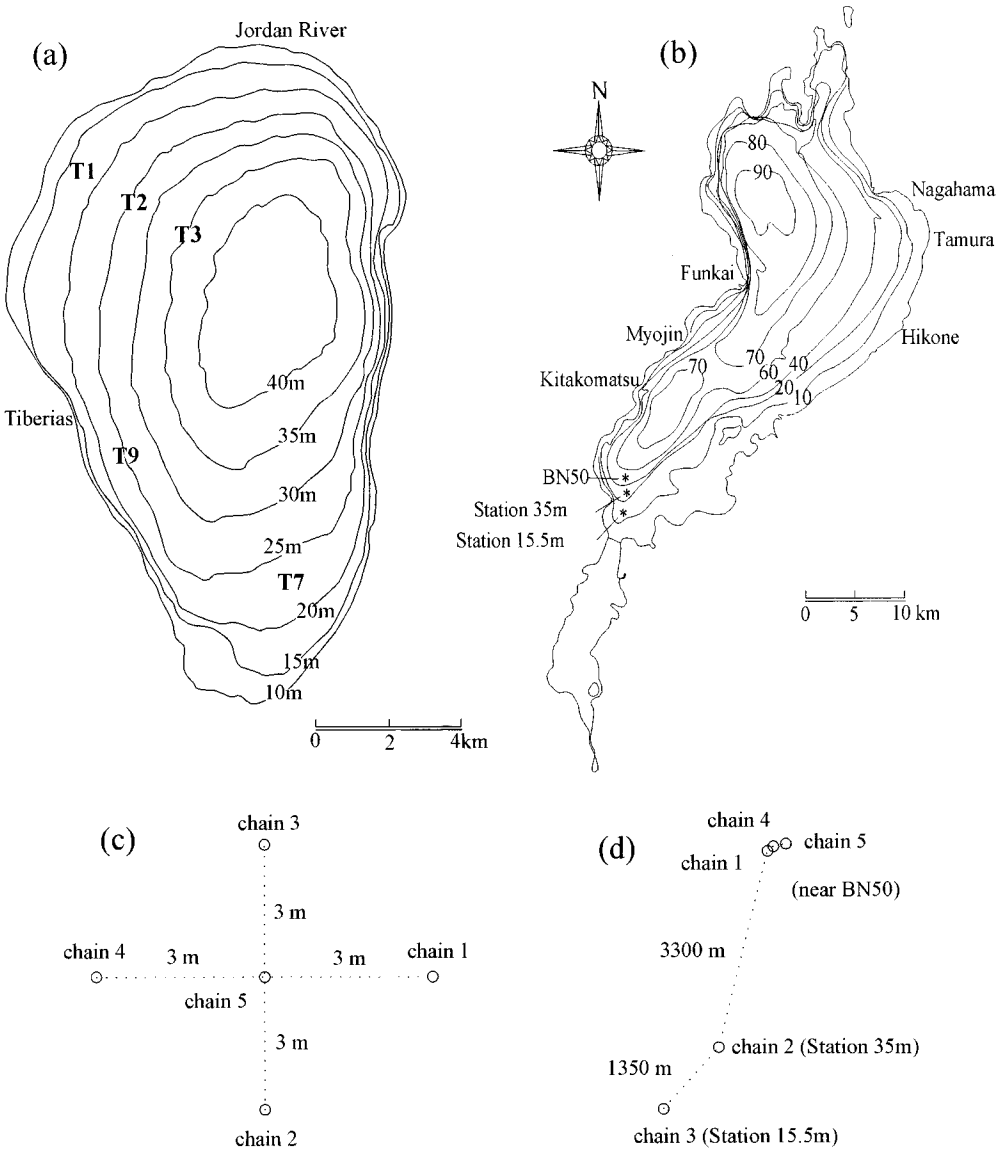

Fig. 1. (a) Lake Kinneret (33°N, 36°E) bathymetry with locations of relevant sampling stations. Observations are presented from thermistor chains deployed at stations T2, T7, and T9 during 1997; at station T3 during 1998; and at stations T1 and T2 during 1999. (b) Lake Biwa (35°N, 136°E) bathymetry with locations of relevant sampling stations. Thermistor chains were deployed near station BN50 during 1992 (c) and near stations BN50, 35m, and 15.5m during 1993 (d). (d) Chains 1 and 4 are 130 m apart; chains 4 and 5 are 205 m apart.

high-frequency internal waves, (2) determine and compare the physical characteristics of the high-frequency internal waves (i.e., wavelength, phase velocity, and spectral domain) by direct observation and through the use of mechanistic theoretical models, and (3) use this information to evaluate the role of high-frequency internal waves as they propagate through the fluid and interact with the lake boundaries. We first present field observations from Lake Kinneret (Israel) and Lake Biwa (Japan) to elucidate the ubiquitous and often periodic nature of high-frequency internal waves. These observations are quantitatively compared to numerical results from linear stability and weakly nonlinear Korteweg–de Vries (KdV) models to evaluate whether the waves can be generated by either shear or nonlinear processes. Finally, we discuss the validity of our numerical/analytical results in direct comparison to field observations and conclude by placing our results within the context of what is presently known about the energetics and mixing within large stratified lakes.

Review of observational methods

The data presented has been extracted from that used in the studies of lakes Biwa and Kinneret by Antenucci et al. (2000) and Saggio and Imberger (1998, 2001). These articles contain rigorous descriptions of the sampling procedures and apparatus. Only a brief summary is provided here. The data

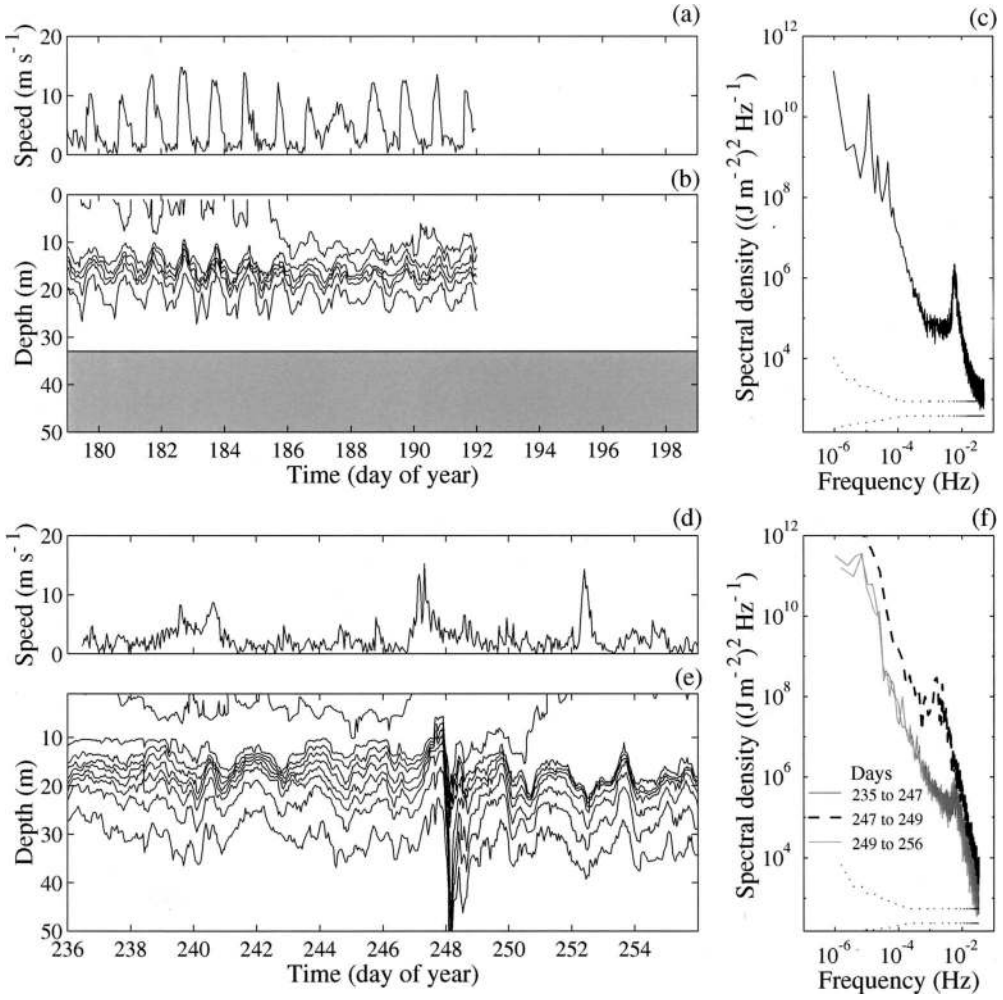

Fig. 2. Observations of wind and isotherm displacement in Lake Kineret (1998) and Lake Biwa (1993) after Antenucci et al. (2000) and Saggio and Imberger (1998), respectively. (a) Wind speed at T3 corrected to 10 m above the water surface; (b) isotherms at 2°C intervals calculated through linear interpolation of thermistor chain data at T3; (c) power spectra of integrated potential energy (Antenucci et al. 2000) from panel b; (d) wind speed at chain 5 (BN50) corrected to 10 m above the water surface; (e) isotherms at 2°C interval calculated through linear interpolation of thermistor chain data at chain 5; (f) power spectra of integrated potential energy from panel e. Data in panels a, b, d, and e have been low-pass–filtered at 1 h. The bottom isotherms in panels b and e are 17°C and 10°C, respectively. In panels c and f, N is $\sim 10^{-2}$ Hz. Spectra have been smoothed in the frequency domain to improve confidence at the 95% level, as shown by the dotted lines.

were recorded in Lake Biwa using thermistor chains with a 15-s sampling interval. The thermistor chains were located near station BN50, deployed in a star-shaped array for 10 d during 1992 (Fig. 1c), and aligned roughly along a transect for 20 d in 1993 (Fig. 1d). In Lake Kinneret, thermistor chain data (Fig. 1a) were recorded for 18 d during 1997 at stations T2 (10-s intervals) and T7 and T9 (120-s intervals), for 14 d during 1998 at station T3 (10-s intervals), and for 17 and 21 d during 1999 at stations T1 and T2 (10-s intervals), respectively. All thermistor chains were sampled with an accuracy of 0.01°C. Individual sensors were spaced at 1-m intervals within the metalimnion and at up to 5-m intervals in the hypolimnion and epilimnion. The thermistor chain data were supplemented with microstructure data collected using a portable flux profiler (PFP) equipped with temperature sensors (0.001°C resolution) and orthogonal two-component laser Doppler velocimeters (0.001 m s^{-1} resolution). Profiling vertically through the water column at a speed of $\sim$0.1 m s^{-1} and a sampling frequency of 100 Hz, the PFP resolved water column structure with vertical scales as small as 1 mm.

Review of study areas

Lake Kinneret (Fig. 1a) is $\sim$22 by 15 km, with a maximum depth of 42 m and an internal Rossby radius typically half the basin width. A June investigation of the basin-scale wave field (Antenucci et al. 2000) revealed the 24-h, vertical mode 1 Kelvin (cyclonic) wave as the dominant response to wind forcing (Fig. 2a–c). Vertical mode 1, 2, and 3 Poincaré

Table 1. Details of PFP deployments and selected data from casts averaged over the time intervals Δt. Overbar denotes depth-averaged quantity. The last two rows contain temporally averaged frequency characteristics of the high-frequency wave events observed using thermistor chains at the indicated locations.

	T1	T2	T3	BN50
No. of PFP casts	5	4	6	3
Δt (min)	14	20	42	26
Depth (m)	16	22	35	50
Vertical bin size (cm)	5	7.5	5	15
$\bar{U}$ (z) (cm s^{-1})	6.8	9.2	2.3	0.24
Maximum U (z) (cm s^{-1})	25	25	11	11
Maximum N (z) (Hz)	1.8×10^{-2}	1.6×10^{-2}	1.4×10^{-2}	1.7×10^{-2}
Frequency of observed energy peak (Hz)	3.8×10^{-3}	3.9×10^{-3}	9.1×10^{-3}	8.6×10^{-3}

(anticyclonic) waves were also observed with periods of 12, 20, and 20 h, respectively (Fig. 2a–c). High-frequency waves were observed by Antenucci and Imberger (2001) to occur in packets at locations where the crest of the 24-h vertical mode 1 Kelvin wave is in phase with the lake's intense diurnal wind forcing. The shear at the crest of the propagating Kelvin wave is thus augmented by wind shear at the base of the epilimnion. These waves were shown to energize a spectral energy peak just below the local N near 10^{-2} Hz (Fig. 2c). An inviscid linear stability analysis demonstrated that unstable modes were possible; however, they did not clearly resolve the growth rate peaks in wavenumber space or rigorously compare the predicted unstable modes to the observed data. Therefore, they were unable to accurately determine the wavelength, direction of propagation, and dissipation timescale of the observed high-frequency waves.

Lake Biwa (Fig. 1b) is ~64 km long with a maximum width of 20 km and a minimum width of only 1.4 km. The main basin has a maximum depth of 104 m and a typical internal Rossby radius of 5.4 km. An investigation of the September internal wave field (Saggio and Imberger 1998) revealed vertical mode 1 and 2 basin-scale Kelvin waves with periods of 2 and 6 d, respectively, and vertical mode 1 basin-scale Poincaré waves with horizontal modes of 1–4 and periods between 12 and 24 h (Fig. 2d–f). High-frequency internal waves associated with internal undular bores and hydraulic jumps were observed near a steepened Kelvin wave after the passage of a typhoon. These large-amplitude high-frequency waves were nonlinear in appearance and energized a spectral energy peak near 10^{-3} (Fig. 2f). Further investigation of the Lake Biwa data set (Maxworthy et al. 1998) revealed vertical mode 2 internal solitary waves that were believed to result from the gravitational collapse of shear instabilities near the crests of the Kelvin waves. These studies on Lake Biwa did not reveal the probability of occurrence of shear instability and, as for Lake Kinneret, the exact character of the wavefield—in particular, the wavelength, direction of propagation, and dissipation timescale of the observed high-frequency waves. These issues for both field studies are addressed here.

Numerical and analytical methods

To interpret and analyze the high-frequency wave domain within the Lake Biwa and Lake Kinneret field records, linear stability and weakly nonlinear models were applied and rigorously compared to the observed field data sets.

Linear stability model—The Taylor–Goldstein equation describes the growth and stability behavior of linear wave modes in inviscid fluids with ambient shear and continuous stratification. The Miles–Howard condition stipulates that the sufficient condition for stability to small perturbations is a local gradient Richardson number Ri $>$ ¼ everywhere in the flow. Here, $\mathrm{Ri} = N^2/(\partial\mathbf{u}/\partial z)^2$, where $\mathbf{u} = (u, v, w)$ is the local fluid velocity. Unstable modes can grow into finite-amplitude perturbations within the flow (cf. Batchelor 1967; Turner 1973).

To determine whether the high-frequency internal wave modes observed in the field data might have occurred as a result of linear shear instability, we used a method similar to that of Sun et al. (1998). However, we retained the viscous and diffusive terms in the governing equations to allow for preferential damping of large wavenumber instabilities (Smyth et al. 1988), and our three-dimensional flow geometry was simplified into two-dimensional horizontal velocity profiles $U(z)$ decomposed from the zonal k and meridional l components along 32 horizontal radii oriented at 11.25° increments. We then recovered the directional nature of the instabilities through combination of the unique solution along each axis in wavenumber space.

We acknowledge that decomposition of a three-dimensional flow field into multiple two-dimensional solution planes precludes three-dimensional primary instabilities. However, these instabilities are not expected in geophysical flows because they have been shown to be restricted to a small region of parameter space where the Reynolds number (Re) is $<$300 (Smyth and Peltier 1990). Here, $\mathrm{Re} = (\mathcal{U}\delta)/\nu$, where $\mathcal{U}$ is a variation in velocity over a length scale δ and ν is the kinematic velocity of the fluid.

We numerically determined the stability of the water column along each axis to forms of the equations of motion subject to infinitesimal wavelike perturbations of the vertical velocity field within a Boussinesq and hydrostatic flow (Eq. 1).

$$\psi(x, z, t) = \Re\{(\hat{\psi}(z)\exp[i\kappa(x - ct)]\} \quad (1)$$

$\kappa = \sqrt{\kappa^2 + l^2}$ is the horizontal wavenumber, $\hat{\psi}(z) = \hat{\psi}_r +$

$i\hat{\psi}_i$ is the complex wavefunction, $c = c_r + ic_i$ is the complex phase speed, and $\omega_i = \kappa c_i > 0$ represents the growth rate of an unstable perturbation.

Mean flow profiles of $N(z)$ and $U(z)$ were obtained by depth averaging observed water column profiles obtained over a finite time interval Δt (Table 1). Sensitivity analysis revealed that depth- and isopycnal-averaged profiles were insignificantly variant as a result of smoothing associated with transforming isopycnal-averaged quantities to the vertical depth coordinate of our stability model. Furthermore, isopycnals are nearly horizontal because Δt is much less that the basin-scale wave period. To reduce the computational demand, the time-averaged profiles were averaged into vertical bins ranging between 5 and 15 cm (Table 1). A matrix eigenvalue method modified after Hogg et al. (2001) was used to solve the sixth order viscous stability equation. As opposed to the methods used by Antenucci and Imberger (2001) or Hogg et al. (2001), in our development we have not assumed inviscid and nondiffusive fluid or made the long wave assumption, respectively. This stability equation is, therefore, a generalization of the Taylor–Goldstein equation that includes viscosity and diffusivity (Koppel 1964).

$$-c^2[\partial^2 - \kappa^2]\hat{\psi} + c[2iK_c(\partial^2 - \kappa^2)^2 + 2U(\partial^2 - \kappa^2) - U_{zz}]\hat{\psi} + [K_c^2(\partial^2 - \kappa^2)^3 - 2iUK_c(\partial^2 - \kappa^2)^2 - 2iU_zK_c\partial(\partial^2 - \kappa^2) - U^2(\partial^2 - \kappa^2) + 2iU_{zzz}K_c\partial + UU_{zz} + iU_{zzzz}K_c - N^2]\hat{\psi} = 0 \quad (2)$$

$K_c = K/\kappa$ and both ∂ and the z subscripts represent the partial derivative with respect to z. Here, K has been defined as ''eddy viscosity'' or ''eddy diffusivity'' parameterization, and a Prandtl number of unity has been assumed.

For the various N and U profiles, ω_i, $\hat{\psi}$, and c were determined over a range of κ. Vertical mode 1–3 solutions were evaluated for wavelengths at 2-m intervals between 1 and 149 m. Along each axis, only the solutions at each wavenumber with the highest growth rate were kept for further analysis. Our results, which involve the determination of the stability of a time-variant flow over a finite time-averaged interval, can be considered exact for $\omega_i \gg 1/\Delta t$ (Smyth and Peltier 1994).

Korteweg–de Vries model—Internal solitary waves can be modeled to first order by the weakly nonlinear KdV equation (Eq. 3).

$$\eta_t + c_o\eta_x + \alpha\eta\eta_x + \beta\eta_{xxx} = 0 \quad (3)$$

$\zeta(x, z, t) \approx \eta(x, t)\hat{\psi}(z)$ is the wave amplitude, c_o is the linear long-wave speed, and subscripts denote differentiation. A balance between nonlinear steepening $\eta\eta_x$ and dispersion η_{xxx} results in waves of permanent form.

The coefficients α and β are known in terms of the water column properties $\rho(z)$ and $U(z)$ and the modal function $\hat{\psi}(z)$ (Eq. 4; Benny 1966).

$$\alpha = \frac{3\int_0^H \rho(c_o - U)^2\hat{\psi}_z^3\,dz}{2\int_0^H \rho(c_o - U)^2\hat{\psi}_z^2\,dz}$$

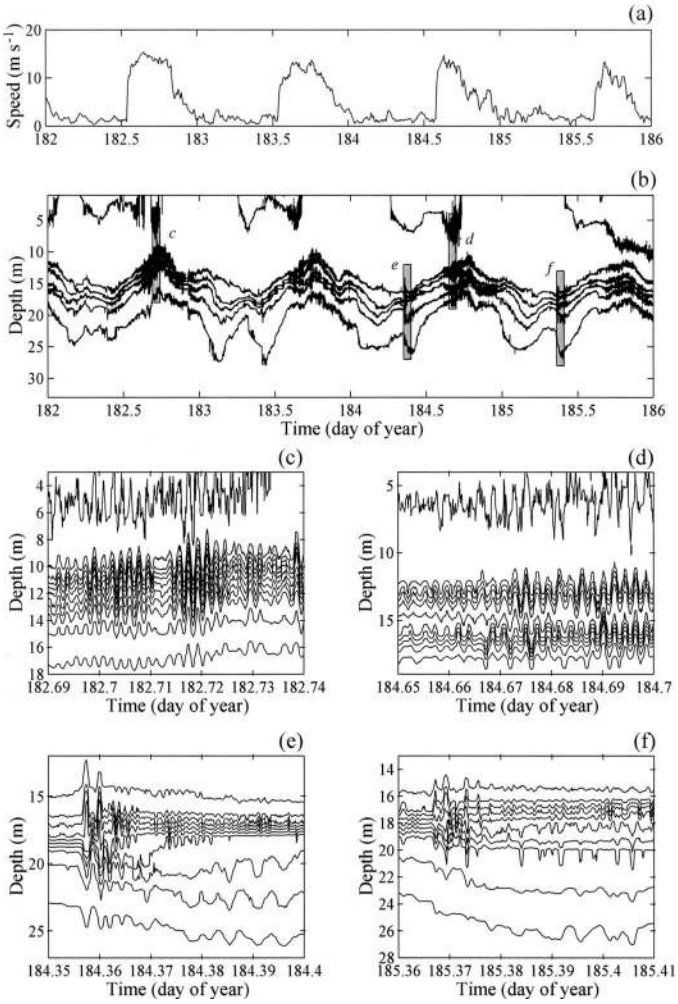

Fig. 3. Observations from station T3 in Lake Kinneret in 1998. (a) Ten-minute average wind speed correct from 1.5 to 10 m, (b) 2°C isotherms for a 4-d observation period, (c) magnified view of shaded region c in panel b showing 1°C isotherms, (d) magnified view of shaded region d in panel b showing 1°C isotherms, (e) magnified view of shaded region e in panel b showing 1°C isotherm, (f) magnified view of shaded region f in panel b showing 1°C isotherms. Wind and temperature data were collected at 10-s intervals, with isotherms calculated through linear interpolation. The bottom isotherm in panel b is 17°C.

$$\beta = \frac{\int_0^H \rho(c_o - U)^2\hat{\psi}^2\,dz}{2\int_0^H \rho(c_o - U)^2\hat{\psi}_z^2\,dz} \quad (4)$$

H is the height of the water column and $\hat{\psi}$ is determined from the numerical solution of Eq. 2 with $\kappa = 0$. Note that in setting $\kappa = 0$, it was also necessary to specify $K = 0$ in order to maintain a finite K_c; otherwise, Eq. 2 will represent modes in an infinitely viscous fluid.

From Eq. 3, the solitary wave solution is Eq. 5 (Benny 1966).

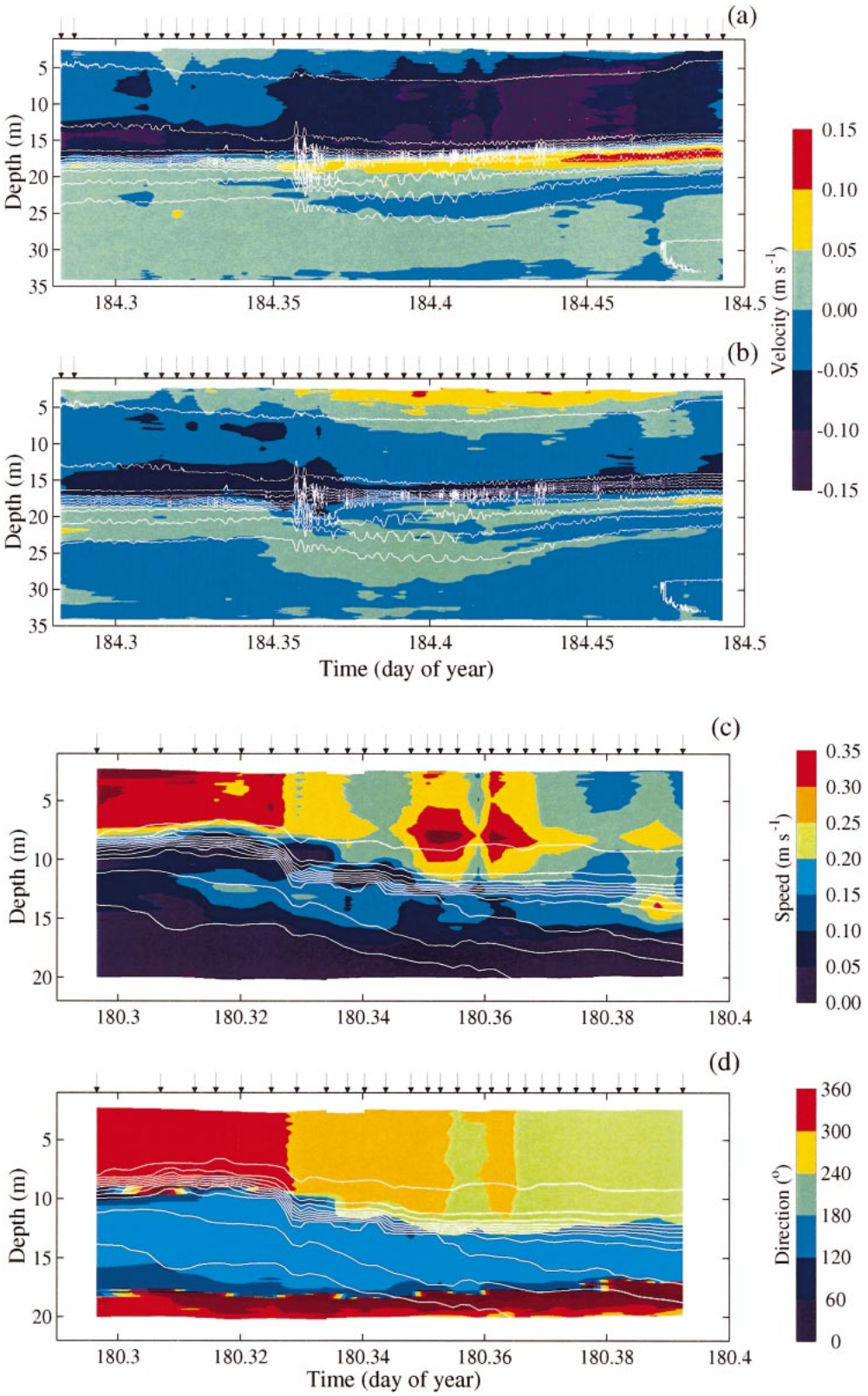

Fig. 4. PFP observations near station T3 in Lake Kinneret (1998) of background temperature and velocity structure during the passage of a vertical mode 2 wave event depicted in Fig. 3e on day 184: (a) isotherms from T3 data collected at 10-s intervals, superposed on contours of current velocity in the north–south direction (north positive) derived from PFP casts as indicated by arrows and averaged into 15-cm vertical bins; (b) isotherms as in panel a, superposed on contours of current

$$\eta(x - c_1 t) = a \operatorname{sech}^2\left(\frac{x - c_1 t}{L}\right) \tag{5}$$

The phase velocity c_1 and horizontal length scale L are given by Eq. 6.

$$c_1 = c_o + \frac{1}{3}\alpha a \qquad L = \sqrt{\frac{12\beta}{a\alpha}} \tag{6}$$

The soliton amplitude is a. Considering the sech^2 solitary wave shape, Holloway (1987) suggests that the soliton wavelength $\lambda \approx 3.6L$.

To apply the continuous KdV theory described above to field observations of finite-amplitude internal waves requires a knowledge of the velocity and density structure of the water column. In practice, this requires an a priori knowledge of the spatial and temporal distribution of the waves to be sampled. Although this might not be a hindrance in large-scale and periodic tidal flows (e.g., Apel et al. 1985), in lakes, these waves are of much smaller scale and do not exhibit a surface signature visible through noninvasive remote sensing (e.g., satellite) techniques. Historically, such limitations on the quality of field data has prevented comparison of the continuous KdV theory described above to field observations of internal solitary waves in lakes. Qualitative or simplified models that neglect mean shear and employ layered approximations of the continuous density profile have been applied (e.g., Hunkins and Fliegel 1973; Farmer 1978).

Vertical mode 1 internal solitary waves can be modeled analytically in a two-layer Boussinesq and hydrostatic flow with no mean shear and of depth h_1 and density ρ_1 over depth h_2 and density ρ_2 using Eq. 6 and Eq. 7, where $c_o = [(g' h_1 h_2)/(h_1 + h_2)]^{1/2}$.

$$\alpha = \frac{3c_o}{2h_1 h_2}(h_1 - h_2) \qquad \beta = \frac{c_o h_1 h_2}{6} \tag{7}$$

Vertical mode 2 internal solitary waves can be modeled using the three-layer theoretical solution for wave celerity by Schmidt and Spigel (2000). In this model, the mode 2 phase speed c_2 is

$$c_2 = c_{o_2}\frac{4}{3}\sqrt{\frac{2a}{h_2}} \qquad c_{o_2} = \sqrt{\frac{gh_2}{4}\left(\frac{\rho_1 - \rho_3}{\rho_3 + \rho_1}\right)} \tag{8}$$

where the speed of an infinitesimal mode 1 wave is c_{o_2}, the upper or lower interface wave amplitude is a, and the ambient fluid is characterized by a middle layer of thickness h_2 and upper and lower layers of density ρ_1 and ρ_3, respectively. The half-wavelength between a and $a/2$ is determined empirically as in Eq. 9.

$$\lambda_{1/2} = 1.98a + 0.48h_2 \tag{9}$$

In this study, we apply the approximate layered models using observations from thermistor chains. Where possible, we supplement these results by applying the continuous KdV model to observations from nearby PFP casts.

Observational results

Ubiquitous nature—Lake Kinneret, 27–30 June 1998 (Fig. 3): Isotherms at station T3 (Fig. 3b) revealed basin-scale wave activity that was in phase with the surface wind forcing (Fig. 3a). Crests of the basin-scale 24-h vertical mode 1 Kelvin wave were observed near days 182.7, 183.7, 184.7, and 185.7, whereas crests of the 12-h vertical mode 1 basin-scale Poincaré wave were observed at the 24-h Kelvin wave crests and troughs. Relatively high-frequency and small-amplitude vertical mode 1 waves, vertically coherent in both phase and frequency (Fig. 3c,d), were apparent riding on the Kelvin wave crests during the periods of intense surface wind forcing. These waves are hypothesized to result from shear instability at the base of the epilimnion (Antenucci and Imberger 2001).

There is also evidence of high-frequency vertical mode 2 waves in this record. The interaction of the 24-h Kelvin wave trough, the 12-h Poincaré wave crest, and the vertical mode 2 20-h Poincaré wave was observed to cause a periodic constriction of the metalimnion. Immediately following this constriction and prior to the subsequent Kelvin wave crest, a packet of vertical mode 2 large-amplitude internal solitary waves with an irregular lower amplitude wave tail was observed (Fig. 3e,f). Unlike the waves of Fig. 3c,d, these waves vary vertically in frequency and phase and are followed by an abrupt splitting of the metalimnion. Analysis of PFP casts (recorded at the times denoted by arrows in Fig. 4a,b) show an overlay of the background velocity field and the isotherm displacements for the wave event in Fig. 3e and are visually consistent with that of an intrusive current or a metalimnion jet driven by the local vertical mode 2 compression or the collapse of a mixed region. The area of high shear above and below the jet is bounded by the irregular wave tail and regions where Ri $<$ ¼ (Fig. 5f). This suggests the possibility of localized shear instability. Some simple calculations can determine whether the mode 2 waves and horizontal jet indeed result from the collapse of a mixed region—a mechanism proposed for Lake Biwa by Maxworthy et al. (1998). From Fig. 4a, we calculate a radially spreading mixed fluid volume of $\pi[(0.1 \text{ m s}^{-1})\ (13{,}000 \text{ s})]^2\ (5 \text{ m}) \approx 2.7 \times 10^7 \text{ m}^3$; this is 0.2% of the lake volume. Assuming a 20% mixing efficiency (Ivey and Imberger 1991), 4×10^8 J of energy are needed to mix this fluid from equal parts of the epilimnion and hypolimnion. This is approximately 4% of the total energy in the internal Kelvin wave field, estimated as 5×10^{10} J (*see* Imberger 1998),

←

velocity in the east–west direction (east positive) derived from PFP casts as in panel a. PFP observations near station T9 in Lake Kinneret (1997) of background temperature and velocity structure during the passage of the steepened wave front depicted in the shaded region of Fig. 7c on day 180: (c) isotherms from T9 data collected at 120-s intervals, superposed on contours of current speed derived from PFP casts, as indicated by arrows, and averaged into 15-cm vertical bins; (d) isotherms as in panel c, superposed on contours of current azimuth direction derived from PFP casts as in panel c.

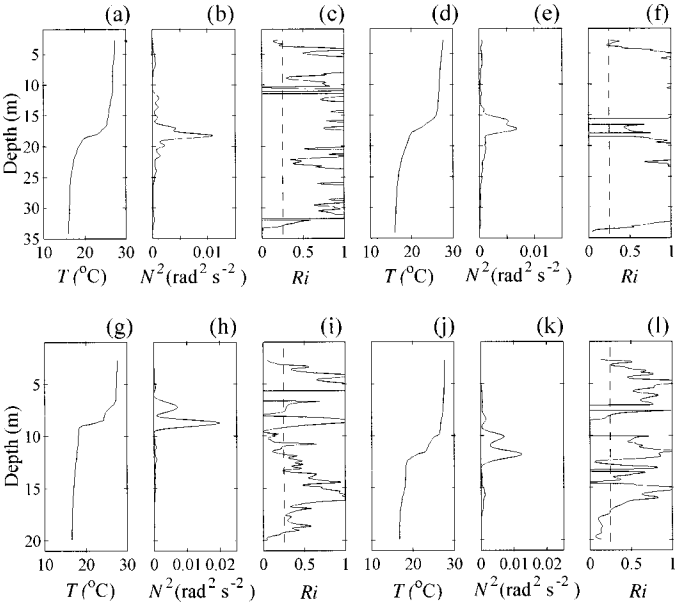

Fig. 5. Time-averaged water column profiles from PFP casts depicted in Fig. 4a,b before the mode 2 wave event on day 184.36—(a) temperature *T*, (b) N^2, (c) Ri—and after the mode 2 wave event on day 184.36—(d) *T*, (e) N^2, (f) Ri. Time-averaged water column profiles from PFP casts depicted in Fig. 4c,d before the steepened wave front on day 180.33—(g) *T*, (h) N^2, (i) Ri—and after the steepened wave front on day 180.33—(j) *T*, (k) N^2, (l) Ri.

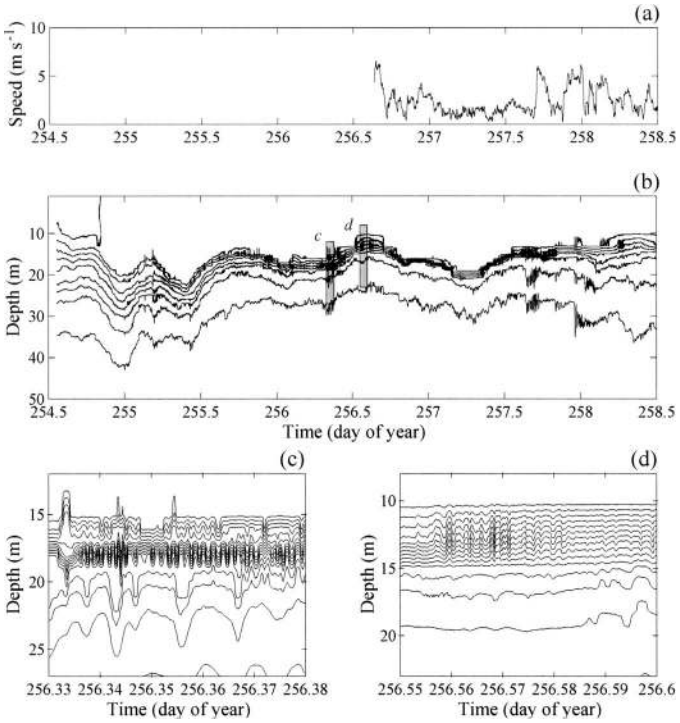

Fig. 6. Observations from chain 5 (BN50) in Lake Biwa in 1992. (a) Wind speed measured at 1.5 m, low-pass–filtered at 10-min intervals; (b) 2°C isotherms for a 4-d observation period; (c) magnified view of shaded region c in panel b showing 1°C isotherms; (d) magnified view of shaded region d in panel b showing 1°C isotherms. Wind and temperature data were collected at 15-s intervals, with isotherms calculated through linear interpolation. The bottom isotherm in panel b is 10°C.

which is a reasonable value. However, if this mixed fluid did originate from the Kelvin wave crest that passed station T3 3.6 h earlier, where has it been in the interim?

Lake Biwa, 11–15 September 1992 (Fig. 6): Isotherms from thermistor chain 5 (Fig. 6b) revealed a period of metalimnion compression, beginning gradually on day 255 and extending until day 258. Saggio and Imberger (1998) described this event as an increase in the buoyancy frequency to a maximum of 0.022 Hz and associated its presence with the passage of a 6-d basin-scale vertical mode 2 Kelvin wave. Throughout this metalimnion compression, the 2-d vertical mode 1 basin-scale Kelvin wave is evident with crests near days 254.5, 256.5, and 258.5. High-frequency vertical mode 1 waves, similar to those in Lake Kinneret, were observed on the Kelvin wave crest at day 256.6 (Fig. 6d) and during moderately strong winds as the metalimnion expanded (days 257.7–258.3). Vertical mode 2 wave events, again remarkably similar to those in Lake Kinneret, were also observed throughout the metalimnion compression (e.g., days 255.2, 256.3 [Fig. 6c], and 258.0).

Nonlinear steepening and boundary interaction—Lake Kinneret, 1–4 July 1997 (Fig. 7): The Kelvin wave crests at station T2 were in phase with the diurnal wind forcing on days 177.7, 178.7, 179.7, and 180.7 (Fig. 7a,b). At station T9 (Fig. 7c), there was a 12-h phase lag with the Kelvin wave crests arriving on days 178.2, 179.2, 180.2, and 181.2. Comparison of Figs. 7b and c over this time interval shows the leading edge of each Kelvin wave trough to have steepened; each wave changed from a sinusoidal shape to one exhibiting a gradual rise in isotherm depth followed by an abrupt descent after the passage of the wave crest. The trough regions exhibited evidence of high-frequency wave activity and metalimnion expansion, but the 2-min sampling interval did not reveal internal solitary waves or other high-frequency waves. Progressing further in a counterclockwise direction, the Kelvin wave crests at station T7 were observed to, once again, possess a sinusoidal shape (Fig. 7d); however, uniformly distributed, relatively high-frequency isotherm oscillations were also observed. These observations suggest a steepening mechanism similar to that observed in long narrow lakes. This nonlinear steepening might be influenced by the nonuniform bathymetry/topography of Lake Kinneret near T9 (cf. Farmer 1978; Mortimer and Horn 1982; Horn et al. 2001).

Data from PFP casts (recorded at the times denoted by arrows in Fig. 4c,d) were linearly interpolated to show an overlay of the background velocity field and the isotherm displacements for the steepened wave front shown as a shaded region in Fig. 7C. Current speeds between 30 and 35 cm s^{-1} were observed as the Kelvin wave crest constricted the local epilimnion thickness (Fig. 4c). These speeds were reduced to 15–20 cm s^{-1} with the passage of the 5-m descending front. Hypolimnetic current speeds were generally <10 cm s^{-1}. The flow was baroclinic in nature, with velocities 180° out of phase across the Kelvin wave crest (Fig. 4d).

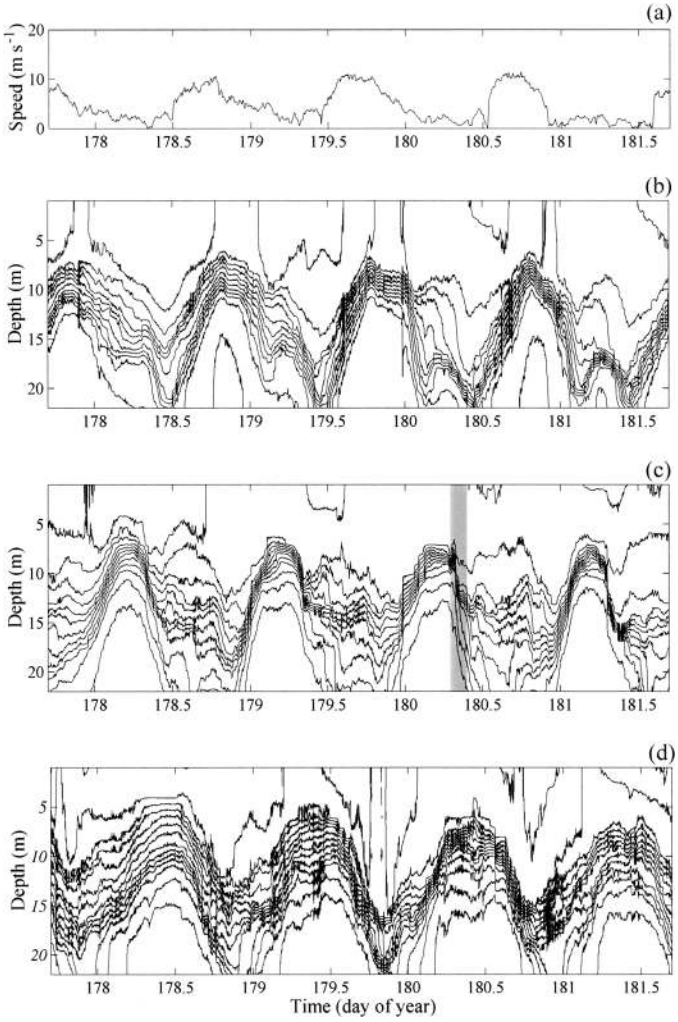

Fig. 7. Observations from Lake Kinneret in 1997. (a) Ten-minute average wind speed corrected from 1.5 to 10 m, (b) station T2, (c) station T9, and (d) station T7 1°C isotherm for a 4-d observation period. Wind and T2 data were collected at 10-s intervals; however, T2 data were decimated to 120-s intervals to match the frequency of data collection at T7 and T9.

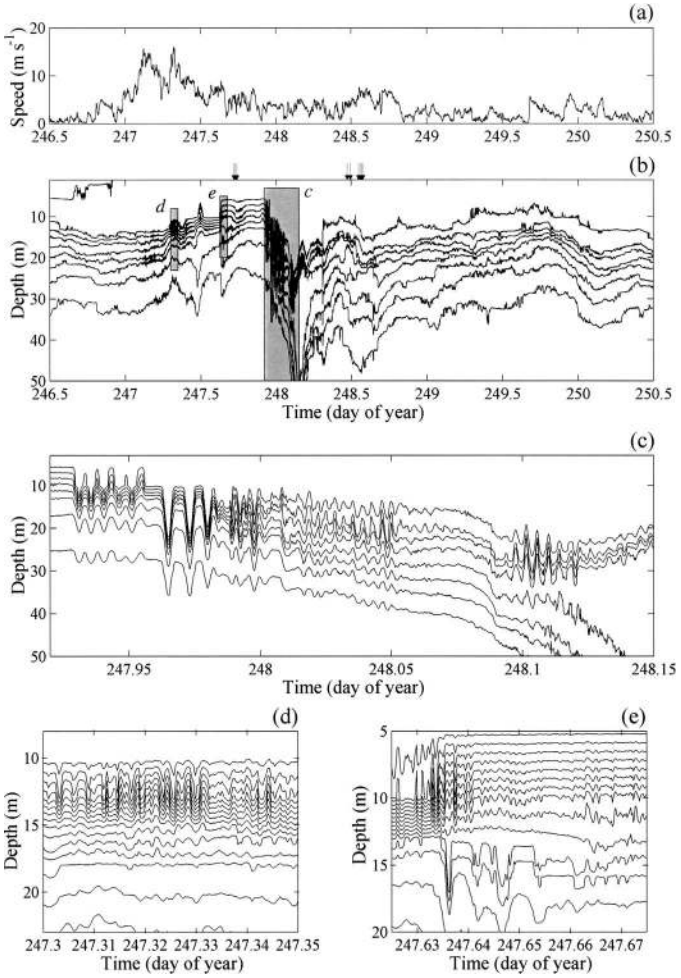

Fig. 8. Observations from chain 5 (BN50) in Lake Biwa in 1993. (a) Wind speed collected at Koshinkyoku Tower, 1 km north of BN50, resampled at 10-min intervals; (b) 2°C isotherms for a 4-d observation period; (c) magnified view of shaded region c in panel b showing 2°C isotherms; (d) magnified view of shaded region d in panel b showing 1°C isotherms; (e) magnified view of shaded region e in panel b showing 1°C isotherms. Temperature data were collected at 15-s intervals, with isotherms calculated through linear interpolation. The bottom isotherm in panels b and c is 10° C. Arrows in panel b denote PFP profiles taken at BN50 on days 247.7194, 247.7292, 247.7375, 248.4736, 248.4951, 248.5493, 248.5597, 248.5681, and 248.5771.

Within the epilimnion, there was a counterclockwise rotation in current direction from NNW through SSW as the Kelvin wave passed. These observations are consistent with the theoretical model of the passage of a Kelvin wave in an idealized three-layer basin matching the dimensions of Lake Kinneret (Antenucci et al. 2000). Averaging data from PFP casts, both before and after the front (Figs. 5g–l), revealed the local Ri to be $<¼$ at the upper and lower bounds of the high-N^2 region, which indicated the possibility of shear instability both above and below the metalimnion.

Lake Biwa, 3–7 September 1993 (Fig. 8): Observations from thermistor chain 5 showed crests associated with the 2-d vertical mode 1 basin-scale Kelvin wave on days 247.8 and 249.8 (Fig. 8b). The first Kelvin wave, observed at the thermistor chain approximately 24 h after the passage of a large typhoon (Fig. 8a), appeared as a gradual increase in the level of the isotherms followed by a rapid descent and a subsequent splitting of the metalimnion. This Kelvin wave is similar in appearance to the steepened Kelvin waves observed in Lake Kinneret at station T9 (Fig. 7c). A magnified view of the abrupt wave front (Fig. 8c) revealed a series of internal steps of depression, each followed by a packet of large-amplitude vertically coherent internal solitary waves and an irregular train of lower amplitude waves. These waves manifest a broad spectral energy peak near 10^{-3} Hz (Fig. 2; Saggio and Imberger 1998) and are identical in character to 15-s observations of a steepened longitudinal seiche in Seneca Lake (*see* fig. 9 in Hunkins and Fliegel 1973). It remains unclear whether these high-frequency waves are generated through nonlinear steepening of basin-scale inter-

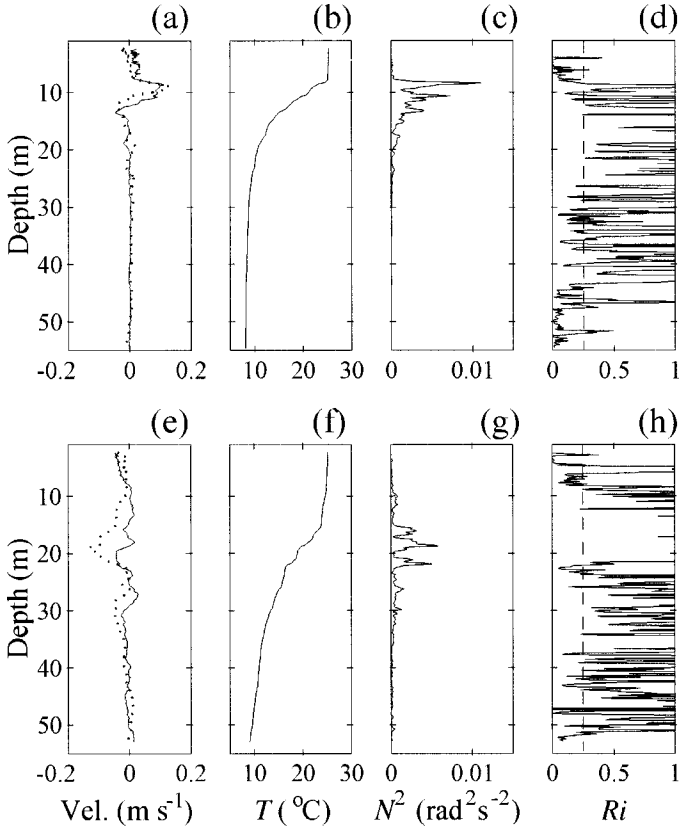

Fig. 9. Background temperature and velocity structure near BN50 in Lake Biwa 1993 as averaged from PFP profiles denoted by arrows in Fig. 8b. (a) North–south (solid line) and east–west (doted line) velocity profiles on day 247 (velocities are positive to the north and east); (b) temperature, *T*, profile on day 247; (c) buoyancy frequency squared on day 247; (d) gradient Richardson number on day 248; (e) north–south (solid line) and east–west (dotted line) velocity profiles on day 248; (f) temperature profile on day 248; (g) buoyancy frequency squared on day 248; (h) gradient Richardson number on day 248.

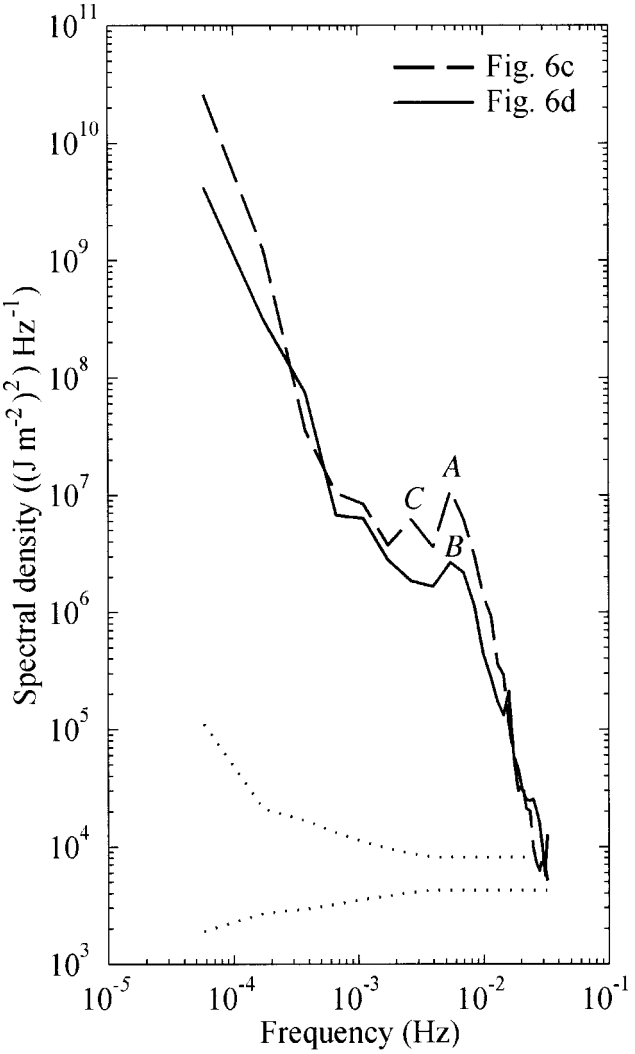

Fig. 10. Spectra of vertically integrated potential energy of Lake Biwa 1992 high-frequency wave events shown in Fig. 6. The spectra were smoothed in the frequency domain to improve statistical confidence, with the 95% confidence level indicated by the dotted lines. *See text* for description of *A*, *B*, and *C*.

nal waves (Horn et al. 2001) or boundary interaction as suggested by Saggio and Imberger (1998).

Data averaged from PFP casts both before and after the passage of the abrupt front (recorded at the times denoted by arrows on Fig. 8b) were used to determine the temporal variation of the background stratification and flow velocity (Fig. 9). Before the front, strong shear was observed across the thermocline at a depth of 10 m (Fig. 9a,b,c). Above this region in the epilimnion, the Ri is $<¼$ (Fig. 9d), which indicates that the high-frequency waves observed through this high-shear region (Fig. 8e) might result from shear instability. Ri $<$ ¼ were also observed through the hypolimnion and benthic boundary layer because of the homogeneous nature of the water column. Once again the passage of the front reduces the intensity of the stratification, abruptly lowering the thermocline depth to approximately 20 m (Fig. 9f,g). Strong shear and Ri $<$ ¼ were also observed at this depth (Fig. 9e,h).

High-frequency wave events similar to those in Fig. 3c–f and Fig. 6c,d were observed throughout the 4-d observation period. For example, vertical mode 1 sinusoidal waves (Fig. 8d) occurred during the intense wind forcing on day 247.3, and vertical mode 2 internal solitary waves preceded an abrupt expansion of the metalimnion and irregular wave tail on day 247.6 (Fig. 8e).

Phase coherence—The close proximity and precise spacing of the thermistor chains deployed in the star-shaped array in Lake Biwa during 1992 (Fig. 1c) allowed the determination of spectral phase coherence correlations for the high-frequency wave events shown in Fig. 6c,d. Because these waves appear in somewhat irregular sinusoidal packets, the observed time-averaged characteristics from phase coherence analysis will yield mean estimates of wavelength and celerity.

Spectral density curves for these high-frequency wave events at chain 5 reveal energy peaks near 10^{-2} Hz (Fig. 10). Phase coherence between chains 3 and 2 and chains 1 and

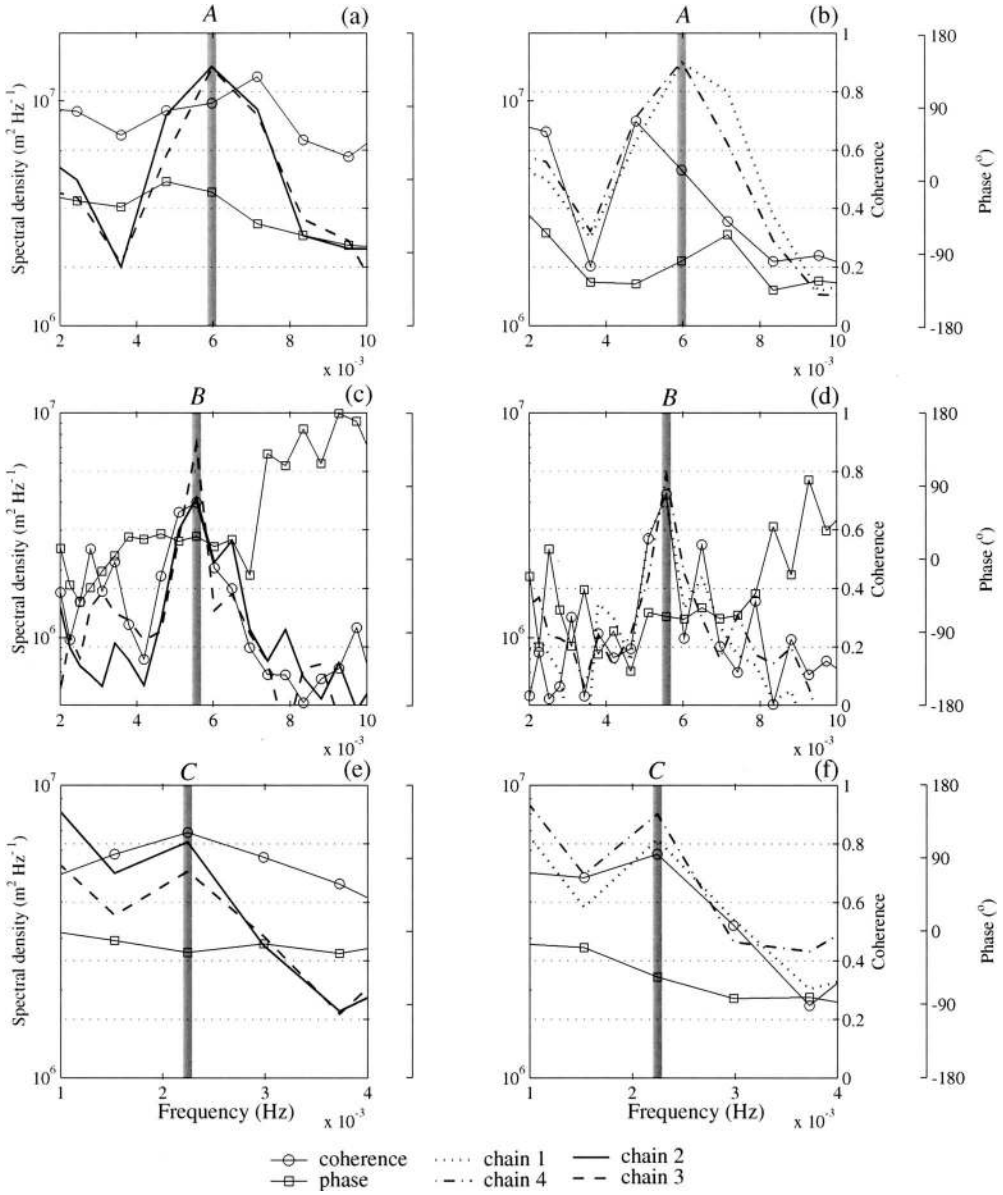

Fig. 11. Orthogonal phase coherence, and energy spectra for the high-frequency wave events identified in Fig. 10. Shading indicates frequency of peaks *A, B,* and *C* as labeled. (a, c, and e) North–south components. (b, d, f) East–west components. Temporal phase is positive to the north and east.

4 show high coherence at the frequencies of the spectral density peaks *A, B,* and *C* (Fig. 11). The 6-m spacing between chain pairs and the temporal phase (Fig. 11) was used to determine the orthogonal components of spectral velocity at each of the spectral density peaks. Division of the spectral velocity components by the spectral frequency yielded the orthogonal wavelength components. The orthogonal components of wavelength and velocity were subsequently combined into vector form, resulting in wavelengths of 21, 28, and 35 m and phase speeds of 13, 16, and 16 cm s^{-1} at peaks *A, B,* and *C,* respectively (Table 2).

Direct observation—Internal solitary waves are not sinusoidal in character and are thus not amenable to phase coherence analysis. However, their physical characteristics can be determined through direct observation because only one positive progressive wave will match the observations at three or more noncollinear thermistor chains.

We considered three large vertical mode 1 waves of depression ordered according to wave amplitude on the steepened Kelvin wave front between days 247.95 and 248 (Fig. 8c) and separated the flow at thermistor chains 1, 4, and 5 (Fig. 1d) into two contiguous layers divided by the 20°C isotherm (Fig. 12). Direct observation gives an average crest-to-crest period of approximately 650 s or a mean temporal frequency $f_t = 1.5 \times 10^{-3}$ Hz. Note that for internal solitary waves, which are nonsinusoidal and irregularly spaced, the temporal frequency is distinct from the spacial

Table 2. Characteristics of the unstable modes from the linear stability analysis results presented in Figs. 15–18. Temporally averaged characteristics of the high-frequency waves shown in Fig. 6c,d and at the spectral peaks in Fig. 10 were determined using phase-coherence correlations across the star-shaped thermistor chain array deployed in Lake Biwa during 1992 (Fig. 1c).

Location	Event type	K ($m^s\ s^{-1}$)	Wavelength (m)	Celerity (cm s^{-1})	Period (s)	Observed period (s)
Most unstable mode						
T1	V1	0	5	20	24	263
T2	V1	0	9	18	51	256
T3	V2	0	8	6	133	110
BM50	V2	0	27	9	300	116
T1	V1	5×10^{-4}	127	15	847	263
T2	V1	10^{-3}	119	14	850	256
Mean ± SD of the most unstable modes beneath the observed spectral energy peaks						
T1	V1	0	37±15	13±0.5	243±485	263
T2	V1	0	36±11	17±0.4	194±538	256
T3	V2	0	9±2	6±0.2	157±48	110
BN50	V2	0	33±12	10±1	340±114	116
Phase coherence observations						
Peak *A*	V2	—	21	13	—	168
Peak *B*	V1	—	28	16	—	180
Peak *C*	V2	—	35	16	—	220

frequency, $f_s = c/\lambda$. Analysis of Figs. 12 and 1d allowed determination of the average wavelength of ~670 m and phase speed of ~180 cm s^{-1} (Table 3). Visual estimates of the relative locations of thermistor chains 1, 4, and 5 are 50% lower than at the locations determined via nondifferential GPS, which indicates that the wavelength and phase speed might be of the order 300 m and 100 cm s^{-1}, respectively.

We also considered the vertical mode 2 internal solitary waves shown in Fig. 6c. Dividing the flow at the 14°C and 24°C isotherms into three contiguous layers (not shown), the wavelength (~65 m) and phase speed (~46 cm s^{-1}) of the leading vertical mode two internal solitary wave in Fig. 6c was determined by direct observation as the wave propagated through the thermistor chain array shown in Fig. 1c (Table 4).

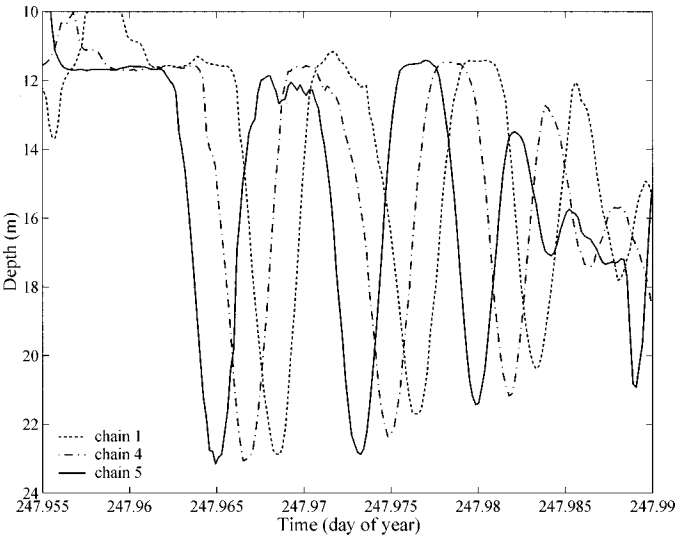

Fig. 12. Detail of Fig. 8c showing vertical mode 1 solitary waves of depression progressing past thermistor chains 1, 4, and 5 (Fig. 1d).

Linear stability results

The observations presented above suggest two classes of high-frequency wave events suitable for linear stability analysis: (1) the vertically coherent mode 1 waves as observed on the crest of a Kelvin wave, henceforth referred to as V1 events, and (2) the vertically incoherent mode 1 waves

Table 3. Comparison of observations and a weakly nonlinear model for the large-amplitude vertical mode 1 internal waves shown in Figs. 8c, 9a–d, 12, and 21a,b. Θ denotes temperature (*see text* for description of other symbols). Designated values were calculated using the quantities given in this table.

Model	Continuous density and shear	Two-layer KdV	Direct observation
h_1 (m)	—	11.75	—
h_2 (m)	—	38.25	—
Θ_1 (°C)	—	26	—
Θ_2 (°C)	—	8	—
ρ_1 (kg m^{-3})	—	996.8	—
ρ_2 (kg m^{-3})	—	999.9	—
a (m)	−11.4	−11.4	−11.4
L (m)	18±3	30	—
λ (m)	64±11	108	~335–670*
c_o (cm s^{-1})	34±2	52	—
c (cm s^{-1})	56±4	69	~90–180
T_s (s)	114†	157†	373±16
f_t (Hz)		—	1.5×10^{-3}

* Calculated by $\lambda = T_s c$.
† Calculated by $T_s = \lambda/c$.

Table 4. Comparison of observations and weakly nonlinear/empirical models for the large-amplitude vertical mode 2 internal waves shown in Figs. 4a,b, 5d–f, and 21c,d (continuous density and shear model) and Fig. 6c (Schmidt and Spigel [2000] model and direct observation). Θ denotes temperature (*see text* for description of other symbols). Designated values were calculated using the quantities given in this table.

Model	Continuous density and shear	Schmidt and Spigel (2000)	Direct observation
h_2 (m)	—	3	—
Θ_1 (°C)	—	24	—
Θ_3 (°C)	—	14	—
ρ_1 (kg m^{-3})	—	997.3	—
ρ_3 (kg m^{-3})	—	999.3	—
a (m)	2.5	2.5	2.5
L (m)	10±7	—	—
λ (m)	35±25	13	~65*
c_o (m s^{-1})	0.16±0.03	0.085	—
c (m s^{-1})	0.23±0.001	0.15	0.46±0.001
T_s (s)	152†	87†	142±20
f_i (Hz)	—	—	1.3×10^{-3}

* Calculated by $\lambda = T_s c$.
† Calculated by $T_s = \lambda/c$.

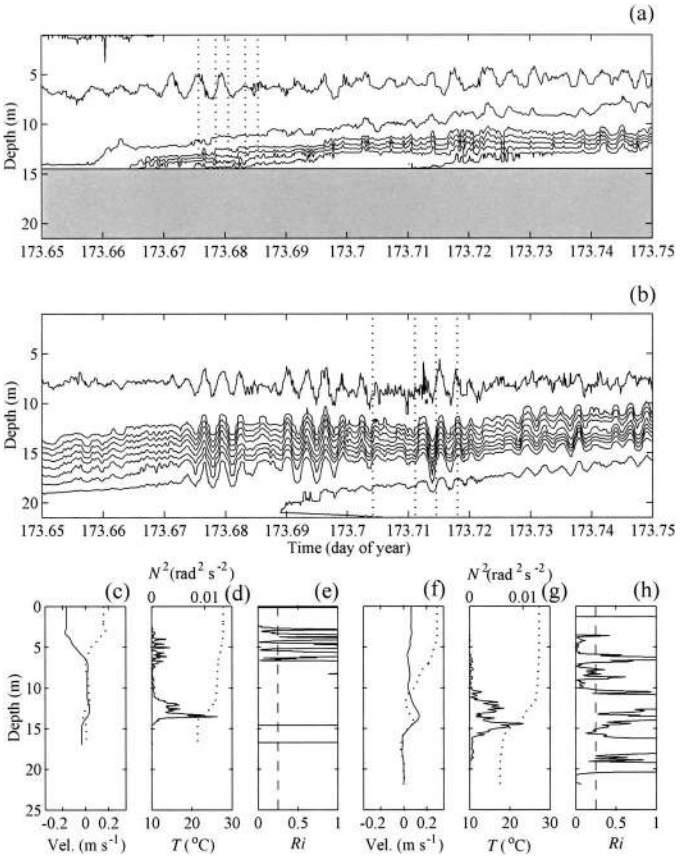

Fig. 13. Observations from Lake Kinneret in 1999. (a) Station T1 1°C isotherm and (b) station T2 1°C isotherms. Data in panels a and b were collected at 10-s intervals; the dotted vertical lines denote PFP casts. (c) North–south (solid line) and east–west (dotted line) velocity profiles from PFP casts at T1 (velocities are positive to the north and east); (d) temperature, *T*, profile (dotted line) and buoyancy frequency squared (solid line) from PFP casts at T1; (e) gradient Richardson number from PFP casts at T1; (f) north–south (solid line) and east–west (dotted line) velocity profiles from PFP casts at T2; (g) temperature profile (dotted line) and buoyancy frequency squared (solid line) from PFP casts at T2; (h) gradient Richardson number from PFP casts at T2.

bounding the jetlike metalimnetic currents that follow vertical mode 2 solitary waves, henceforth referred to as V2 events. To perform a linear stability analysis on events of this type, we require sufficient consecutive PFP casts to establish mean profiles of background density and horizontal velocity while the waves are observed at a particular thermistor chain. The linear stability model was thus applied to the V2 wave events at T3 and BN50 (Figs. 4a,b, 5d–f and 8b,e, 9a–d, respectively) and V1 wave events at T1 and T2 during 1999 in Lake Kinneret (Fig. 13). The lack of PFP casts during the V1 wave events presented thus far has required recourse to 1999 observations. During the passage of these V1 wave events, the water column at T1 and T2 (Fig. 13) exhibited a strong advective horizontal velocity in the epilimnion to a depth of 8 m, a thermocline near 15 m in depth, and Ri $<$ ¼ within the epilimnion and benthic boundary layer. For a rigorous description of the mean flow characteristics observed during the passage of the high-frequency waves depicted in Fig. 13, the reader is referred to Antenucci and Imberger (2001). Figure 14 shows a plan view of the horizonal velocity vector field for each of the V1 and V2 events.

Results are presented in Figs. 15–18 for linear stability solutions of the V1 and V2 events with $0 \leq K \leq 10^{-3}$ m^2 s^{-1}. For each event, the top panels (a, d) show the maximum growth rate in wavenumber space, the right panels (b, e) compare the frequency domain of the maximum growth rate at each wavenumber to the observed isotherm displacement spectra, and the bottom panels (c, f) show the growth rate at each wavelength. Instabilities within the shaded region of panels b and e in Figs. 15–18 have growth periods greater than the period over which the background flow is averaged from PFP casts (i.e., $[\kappa c_i]^{-1} > \Delta t$); thus, solutions within these regions must be interpreted with caution. These solutions are valid if the shearing stress is maintained longer than $(\kappa c_i)^{-1}$. In the present case, this is likely because we are concerned with maximum growth periods of ~60 min (Fig. 15b,e), yet coherent waves persist for ~10 h (e.g., Fig. 3).

For $K = 0$, Figs. 15 and 16 show that the maximum growth rate in wavenumber space is highest in the direction of the mean flow (Fig. 14). This one-sided advective nature is consistent with what would be expected for either a Kelvin–Helmholtz or asymmetrical Holmboe instability (Lawrence et al. 1998). For the V2 wave events (Fig. 15), the frequencies of these unstable modes are between 10^{-3} and 10^{-2} Hz, which corresponds to the high-frequency band associated with the observed vertically incoherent internal waves. These instabilities have wavelengths between 5 and 15 m and 15 and 35 m at T3 and BN50, respectively. The frequency bandwidth and wavelength of these unstable modes are consistent with the observed peak in spectral energy and the phase coherence observations from the similar wave events observed in Lake Biwa (Tables 1, 2). For the

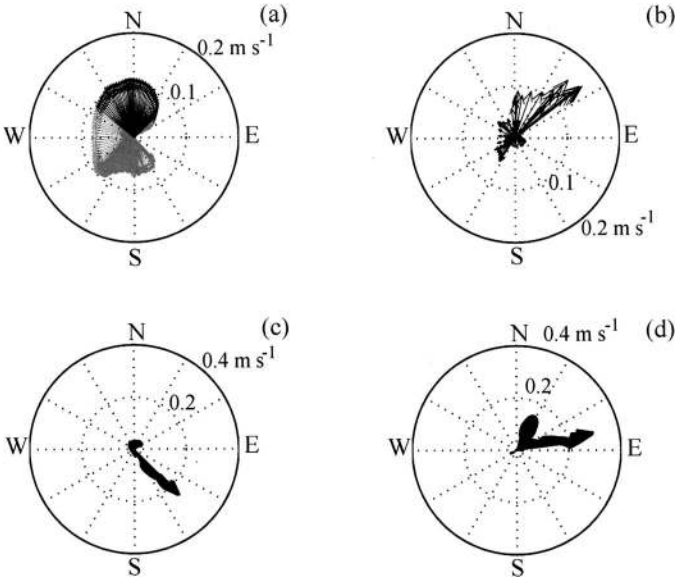

Fig. 14. Plan view of horizontal velocity vectors at (a) T3 from Fig. 4a,b; (b) BN50 from Fig. 9a; (c) T1 from Fig. 13c; and (d) T2 from Fig. 13f. In panel a, the black (north) vectors are located through the metalimnion.

V1 wave events (Fig. 16), the maximum growth rate increases exponentially in shape from low values near 10^{-3} Hz to a super-N peak between 10^{-2} and 10^{-1} Hz followed by a rapid decline thereafter with increasing frequency. The fastest growing instabilities are approximately an order of magnitude in frequency space above the frequency bandwidth of the observed vertically coherent internal waves. At T1 and T2, the most unstable instabilities have wavelengths between 5 and 10 m and 5 and 20 m, respectively.

The spectral gap between the observed high-frequency V1 wave events and the unstable modes predicted via linear stability analysis implies a deficiency in the stability model. This discrepancy may not be attributed to the influence of the local N cutoff on the observed high-frequency waves. Both the moored thermistor chain observations and the linear stability results are Eulerian with respect to the flow field and are thus subject to Doppler shifting (e.g., Garrett and Munk 1979).

To examine whether the spurious high-frequency linear instabilities associated with the V1 wave events can be damped by viscosity and diffusion, we repeated the linear stability analysis with increased values of K. Molecular effects were found to be negligible with no significant change in the wavenumber (or frequency) of the fastest growing modes with $K \leq 10^{-5}$ m^2 s^{-1} (not shown). This is in agreement with the work of others for Re $< \sim$300 (e.g., Nishida and Yoshida 1987; Smyth et al. 1988). A transition region is identified with $K = 2 \times 10^{-4}$ and $K = 5 \times 10^{-4}$ m^2 s^{-1} at T1 and T2, respectively (Fig. 17). These augmented values of K decrease the region of growth of unstable modes for $\kappa > 2$ rad m^{-1} (Fig. 17a,d). Furthermore, the growth rates of instabilities with frequencies $>10^{-2}$ Hz are slightly reduced while those at frequencies $<10^{-2}$ show an increase in growth rate (Fig. 17b,e). These lower frequency instabilities have wavelengths of $\sim$100 m (Fig. 17c,f). An increase in growth rate with increasing viscosity or with increasing stratification and Re < 300 have been shown to be necessary conditions of the primary instabilities to be three-dimensional in character (Smyth and Peltier 1990). However, at T1 and T2 within the shear layer, Re $\approx 10^6$ (Fig. 13); thus, three-dimensional primary instabilities are not expected. As K is further increased to 5×10^{-4} and 10^{-3} m^2 s^{-1} at T1 and T2, respectively (Fig. 18), the transition becomes complete. The most unstable modes have frequencies near 10^{-3} Hz and wavelengths $>$100 m. However, these modes are physically inconsistent with the phase coherence observations from Lake Biwa. The dramatic increase in growth rate with increasing K suggests that these solutions might be numerically unstable.

Water column microstructure profiles—The horizontal current speed, density, and wavefunction profiles of the most unstable modes are shown in Figs. 19 and 20. These can be compared to vertical velocity profiles from the PFP casts (Figs. 19b,f, 20b,g), which were averaged temporally over Δt to minimize fluctuations resulting from irreversible turbulent motions. With $K = 0$, the $\hat{\psi}$ (Figs. 19c,g, 20c,h) and observed w profiles show remarkable similarity in the variation of vertical modal structure with depth. Local maximum values of $\hat{\psi}$ are shown to occur within thin layers where Ri $< \frac{1}{4}$. It is significant to stress that these profiles are independent; that is, $\hat{\psi}$ was calculated using density and *horizontal* velocity profiles only. The most unstable modes with augmented values of K (Fig. 18b,e) exhibit $\hat{\psi}$ profiles (Fig. 20d,i), which are visually inconsistent with the observed variation of vertical modal structure with depth. For these modes, the occurrence of local maxima in $\hat{\psi}$ does not appear to be correlated to the local Ri.

Although the density profiles are generally similar, the horizontal current speed profiles varied between V1 and V2 events. At T1 and T2, the velocities are greatest in the upper mixed layer and a tendency toward the Kelvin–Helmholtz or Holmboe mode (as determined by comparison of the thickness of the local density/temperature gradient region relative to the local shear gradient region, e.g., Lawrence et al. [1998]) was not evident. At T3 and BN50, horizontal velocities were greatest in jets located within the metalimnion. This vertical mode 2 structure was also evident in the isotherms (Fig. 3e,f) and w and $\hat{\psi}$ profiles.

The scale and nature of the unstable regions was determined by calculation of the Thorpe length scale L_T. The vertical displacements required to monotonize the temporally averaged temperature profiles were resampled as an average over 0.05-m intervals, and the root mean square (RMS) displacement was evaluated over 0.5-m vertical bins (Figs. 19d,h, 20e,j). Overturns are shown to have occurred at depths consistent with those of maximum $\hat{\psi}$ and w and over length scales of $0.25 \leq L_T \leq 1.5$ m. These L_T observations are similar in magnitude and position within the water column to L_T observations associated with billowlike structures in the epilimnion of Loch Ness (Thorpe 1978).

Nonlinear wave model results

We have presented observations of large-amplitude waves similar to those produced by nonlinear steepening of basin-scale waves or boundary interaction (e.g., Figs. 7, 8c) and excitation by intrusions and gravity currents (e.g., Fig. 4a), three of the excitation mechanisms described in the introduction.

Equations 2, 4, and 6 were used to calculate the celerity and wavelength of solitary waves that can be supported by the water column profiles shown in Figs. 5d–f and 9a–d. Vertical mode 1 (Fig. 21a,b) and 2 (Fig. 21c,d) solutions along each of the 32 radial axes were averaged over a range of a. Note the linear dependence of c on a, which accounts for the intrapacket rank ordering of solitons by amplitude (e.g., Fig. 8), and the inverse power dependence of λ on a as required by Eq. 6.

The standard deviation, as indicated by error bars about the mean λ and c in Fig. 21, is a measure of the influence of ambient shear on the wave kinematics at a particular a. This is because with $\kappa = 0$, the shear profile input to the linear stability model is the only parameter that is variable along each radial axis. Unlike oceanic observations (e.g., Apel et al. 1985), these results show that the wavelength of small-amplitude solitary waves and the celerity of large-amplitude solitary waves are strongly modified by in-plane vertical shear.

We applied the two- and three-layer models (Eqs. 6–9) to the three large vertical mode 1 waves of depression ordered according to wave amplitude on the steepened Kelvin wave front between days 247.95 and 248 (Figs. 8c, 12) and the leading vertical mode 2 internal solitary waves shown in the wave event of Fig. 6c, respectively. The density of each layer was estimated from the temperature observations using a standard UNESCO polynomial. Using the amplitude estimates of -11.4 and 2.5 m and coefficients as presented in Tables 3 and 4, wavelengths of 108 and 13 m and celerities of 69 and 9 cm s^{-1} were calculated for the vertical mode 1 and 2 waves, respectively. Tables 3 and 4 show these results to be of the same order as those determined from direct observations and with the continuous stratification KdV model.

Discussion

We have presented observations of ubiquitous high-frequency internal wave events. Both large-amplitude and sinusoidal waves were observed. The large-amplitude waves were found to be reasonably described by nonlinear models. The sinusoidal waves were categorized within two distinct classes: vertically coherent vertical mode 1 waves (V1 events), which were associated with strong wind shear in the surface layer, and vertically incoherent mode 1 and mode 2 internal waves bordering thermocline jets (V2 events). For both classes of sinusoidal waves, the local Ri was $<¼$ and unstable modes were predicted via linear stability analysis, suggesting that the wave packets might be energized through shear instability. Interestingly, the V2 events were well modeled within the frequency domain by the linear stability model, whereas the V1 events were modeled at frequencies an order of magnitude greater than observed. Below, we present several theories that address this apparent dichotomy and generalize our results to the context of what is presently known about the energetics and mixing within large stratified lakes.

Coherence and turbulence—Microstructure observations in Lake Kinneret have identified two turbulent regimes within the metalimnion (*see* figs. 9 and 10 in Saggio and Imberger 2001): (1) energetic turbulence ($\varepsilon \approx 10^{-6}$ m^2 s^{-3}, where ε denotes dissipation of turbulent kinetic energy) and elevated buoyancy flux, which was energized by shear production, and (2) less energetic turbulence ($\varepsilon \approx 10^{-8}$ m^2 s^{-3}) that was characterized by low strain ratios and very small scale overturns, indicating that the turbulence was possibly energized by wave–wave interaction. The temporal and spatial locations of these microstructure observations suggest that the V1 wave events are associated with the energetic shear-driven turbulence, whereas the V2 wave events correspond to the less energetic small-scale turbulence. These observed dissipation rates are used below to calculate dissipation timescales.

A distinguishing feature of the V1 and V2 wave events is that the V1 events are vertically coherent, whereas the V2 events are not. It follows that the V1 events might result from classical vertically coherent shear instability in an approximate two-layered system (e.g., Lawrence et al. 1998), whereas the V2 events, which occur on the internal interfaces of a three-layer mean flow, are rendered vertically incoherent as a result of destructive wave–wave interaction between instabilities on the upper and lower interfaces. The turbulence characteristics from Saggio and Imberger (2001) and the isotherm displacement and velocity measurements presented herein are consistent with this hypothesis.

Growth rate versus decay rate—The flow within the metalimnion of Lake Kinneret is predominantly laminar (Saggio and Imberger 2001). It can thus be argued that rapidly growing shear instabilities that sporadically evolve into turbulent events grow in a laminar environment; therefore, the application of an eddy viscosity to damp the spurious high-frequency modes (i.e., $K \gg \nu$) might be physically unrealistic. Furthermore, the most unstable modes in Fig. 16 (which have growth rates an order of magnitude greater than those in Fig. 15) might evolve rapidly into gravitationally unstable structures whose decomposition fuels the energetic shear-driven turbulence. The influence of dissipation on the growth of these unstable modes might, therefore, be best examined through comparison of the energy dissipation rate $1/T_D = \varepsilon/E_{tot}$ and the growth rate κc_i for instabilities of various wavelengths, where T_D is the energy dissipation timescale and E_{tot} is the sum of potential and kinetic energy in the unstable waveform. If the spurious V1 modes predicted through linear stability analysis occur in a frequency bandwidth where the decay rates of the unstable modes are greater than the growth rates, then observed waves are not expected.

During the initial linear stages of growth, E_{tot} can be estimated assuming a linear sinusoidal waveform; a waveform

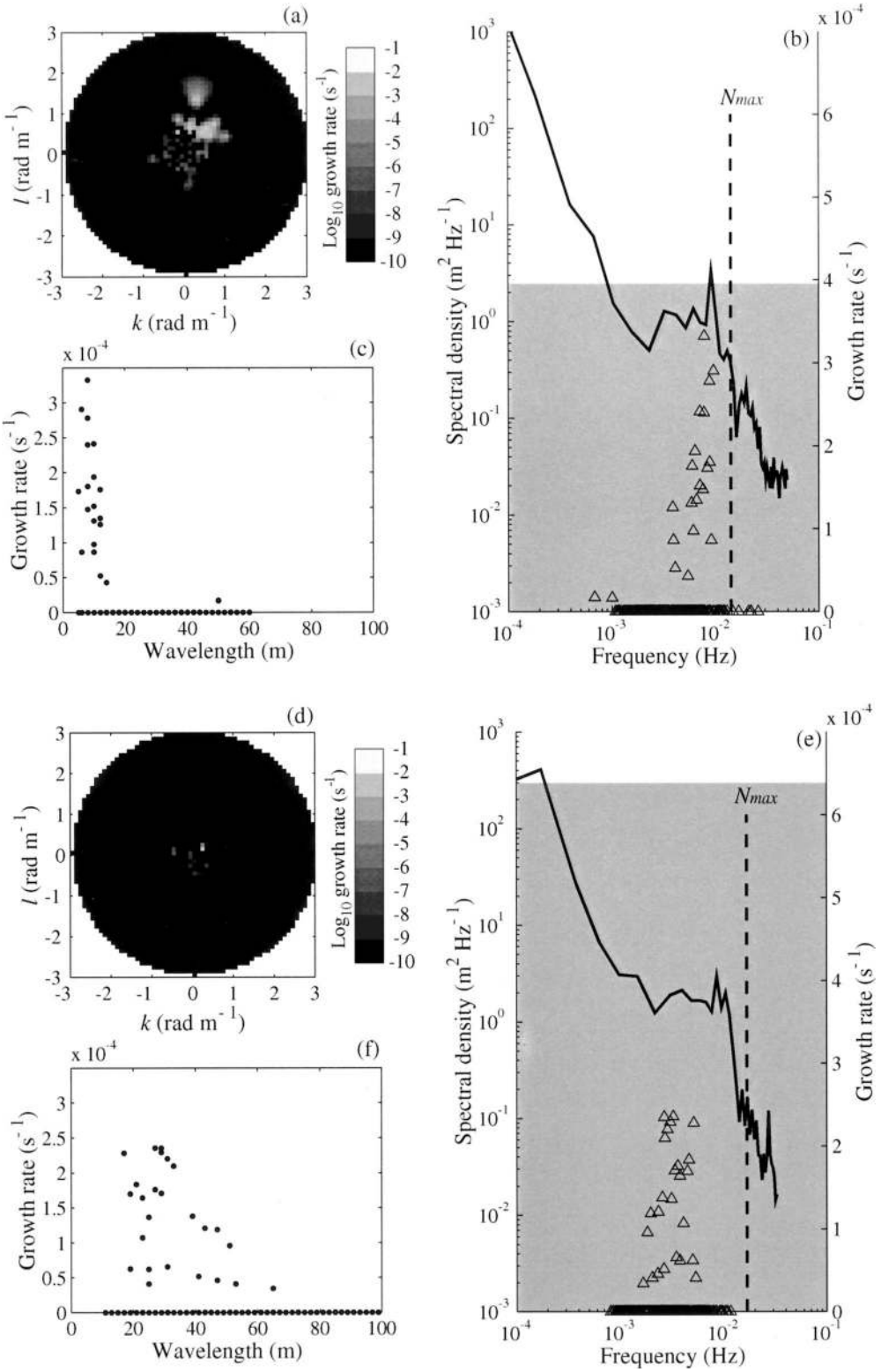

Fig. 15. Linear stability results with $K = 0$ (inviscid) for V2 wave events in Lake Kinneret at T3 (Figs. 4a,b, 5d–f) and Lake Biwa at BN50 (Figs. 8b, 9a-d). Maximum growth rate of unstable modes in horizontal wavenumber space at T3 (a) and BN50 (d). Zonal and meridional wavenumbers are denoted by k and l, respectively. Growth rate in frequency c_r/λ space for the most unstable modes at each wavenumber (hollow triangles) at T3 (b) and BN50 (e). Also plotted in panels b and e are the 22°C and 17°C, respectively, isotherm displacement spectra as observed from a moored thermistor chain at each location (solid line); the region where the growth period $1/\kappa c_i$ is greater

demonstrated using both theoretical (Holmboe 1962; Batchelor 1967) and direct numerical models (Smyth et al. 1988). From the sinusoidal waveform, Holmboe and Kelvin–Helmoltz modes evolve to finite amplitude through harmonic amplification and exponential monotonic growth, respectively (Holmboe 1962; Batchelor 1967; Smyth et al. 1988). A linear, two-dimensional sinusoidal wave in a continuously stratified fluid is described in modal form as $w = w_o \cos \kappa x \sin mz e^{i\omega t}$, where w is the vertical velocity component (positive upward), w_o is the maximum vertical particle speed, t is time, and κ and m are the horizontal and vertical wavenumbers, respectively (e.g., Turner 1973). Following Gill (1982), the potential energy of this vertical mode 1 wave was approximated through integration of the perturbation density field over one wavelength, where t was set equal to one quarter of the oscillation period such that all energy is in the potential form of Eq. 10.

$$E_{\text{tot}} \approx \frac{1}{8}\rho_o w_o^2 \lambda H\left(\frac{\lambda^2}{4H^2} + 1\right) \tag{10}$$

Here, H is the vertical thickness of the standing wave cell. The dissipation timescale was then calculated as

$$T_{\text{D}} \approx \frac{E_{\text{tot}}}{\varepsilon_v} = \frac{w_o^2}{8\varepsilon}\left(\frac{\lambda^2}{4H^2} + 1\right) \tag{11}$$

where $\varepsilon_v = \varepsilon \rho_o H \lambda$ is the volumetric dissipation rate. This result is consistent with that derived by LeBlond (1966) for linear waves of the form given in Eq. 1.

The decay rate ($1/T_{\text{D}}$) and growth rate of the fastest growing mode for each wavelength at T1 and T2 with $K = 0$ (i.e., Fig. 16) are compared in Fig. 23. In Eq. 11, H and w_o were obtained from the observed vertical velocity profiles (Fig. 20), and an upper bound of $\varepsilon \approx 10^{-6}$ m^2 s^{-3} was estimated using the results of Saggio and Imberger (2001) discussed above. An overlay of the observed spectral density curve from Fig. 16b,e indicates that instabilities at frequencies $>10^{-2}$ Hz might dissipate their energy at a rate faster than they will grow; hence, waves would not be observed at these frequencies. Conversely, waves with frequencies between 10^{-3} and 10^{-2} Hz might grow faster than they decay, which would result in the growth of instabilities that match the frequency bandwidth of the observed spectral energy peak.

Thermocline trapping—An alternative explanation, encompassing internal wave dynamics, has been proposed for the observed rise in spectral energy just below the maximum N (Mortimer et al. 1968; Garrett and Munk 1975). For a water column with variable stratification and, in particular, with a thermocline (subsurface region of pronounced maximum N), internal waves can be trapped within the layer of the water column where N exceeds the wave frequency (cf. Groen 1948; Eckart 1960; Turner 1973). This wave trapping has the effect of retaining energy in the region of the frequency domain where $N_{\min} < f < N_{\max}$ (see chapt. 12 in Eckart 1960): hence, the observed energy peak just below the maximum N. If the unstable modes predicted via linear stability analysis are oscillatory in nature, this trapping will prevent amplification of a sinusoidal waveform with wavelength close to that for which the growth rate is a maximum (i.e., at the super-N growth rate peak, see p. 517 in Batchelor 1967). This, in turn, will limit the oscillatory waves to the "allowed" $N_{\min} < f < N_{\max}$ frequency range. Desaubies (1975) has shown that this theoretical model reproduces the sub-N energy peak observed in oceanic internal wave spectra subject to a particular observed N profile.

Eddy coefficients—To determine the appropriateness of the values of K applied in Figs. 17 and 18, we used the ε observations from Saggio and Imberger (2001) to obtain estimates of turbulent diffusivity (K_ρ) during the high-frequency wave events. The Ri model by Imberger and Yeates (unpubl. data) and the models of Osbron (1980) and Barry et al. (2001) based on $\varepsilon - N$ were used to calculate K_ρ (Fig. 22). We have used a constant ε throughout the water column obtained from observations within the upper mixed layer and metalimnion; therefore, the $\varepsilon - N$ models are only valid through this region. Note the variable nature of K_ρ throughout the water column, which suggest that our use of a depth-invariant K is physically unrealistic; therefore, overdamping could be the cause of the suspected numerical instability when K is large. Regardless, from Fig. 18, the magnitude of K required to suppress the spurious high-frequency instabilities above 10^{-2} Hz is approximately 5×10^{-4} and 10^{-3} m^2 s^{-2} at T1 and T2, respectively. These values of K are of the same order as those predicted using the three observational models (Fig. 22). At T3 and BN50, the observational K is below 10^{-5} m^2 s^{-1}, the level at which we found no significant influence of K on the unstable modes; hence, our choice of negligible K in our stability simulations for these events is justified.

Energy flux paths—Localized shear instability has been observed to be the dominant dissipation mechanism within the Lake Kinneret interior (Saggio and Imberger 2001). Using simple energy models, Imberger (1998) and Saggio and Imberger (1998) demonstrated that this interior metalimnetic dissipation plays a negligible role in the dissipation of basin-scale internal wave energy and is consequently insignificant in the overall energy budget of large stratified lakes. Observations of the spatial distribution of turbulent dissipation in wind-forced lakes (Imberger 1998; Wüest et al. 2000) show benthic boundary layer (BBL) dissipation to be an order of magnitude more significant than interior dissipation and demonstrate that BBL dissipation is sufficient to damp basin-

←

than the averaging period Δ_t (shaded region); and the maximum N (dashed vertical line). The spectra were smoothed in the frequency domain to improve statistical confidence. Maximum growth rate of unstable modes versus wavelength at T3 (c) and BN50 (f). Physical properties of the unstable modes are given in Table 2.

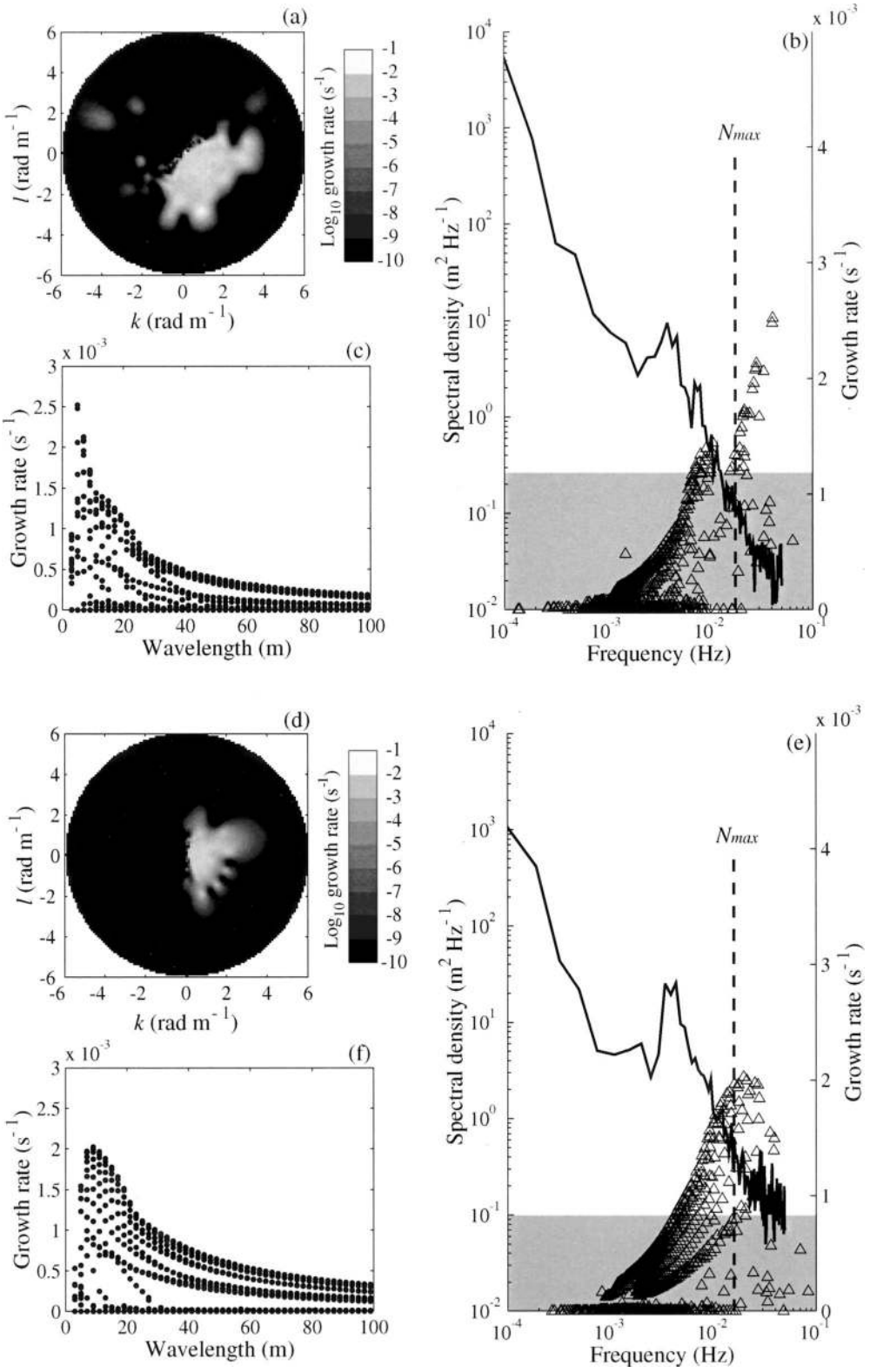

Fig. 16. Linear stability results with $K = 0$ (inviscid) for V1 wave events in Lake Kinneret at T1 (Fig. 13a,c–e) and T2 (Fig. 13b,f–h). Maximum growth rate of unstable modes in horizontal wavenumber space at T1 (a) and T2 (d). Zonal and meridional wavenumbers are denoted by k and l, respectively. Growth rate in frequency c_r/λ space for the most unstable modes at each wavenumber (hollow triangles) at T1 (b) an T2 (e). Also plotted in panels b and e are the 27°C isotherm displacement spectra as observed from a moored thermistor chain at each location (solid line), the

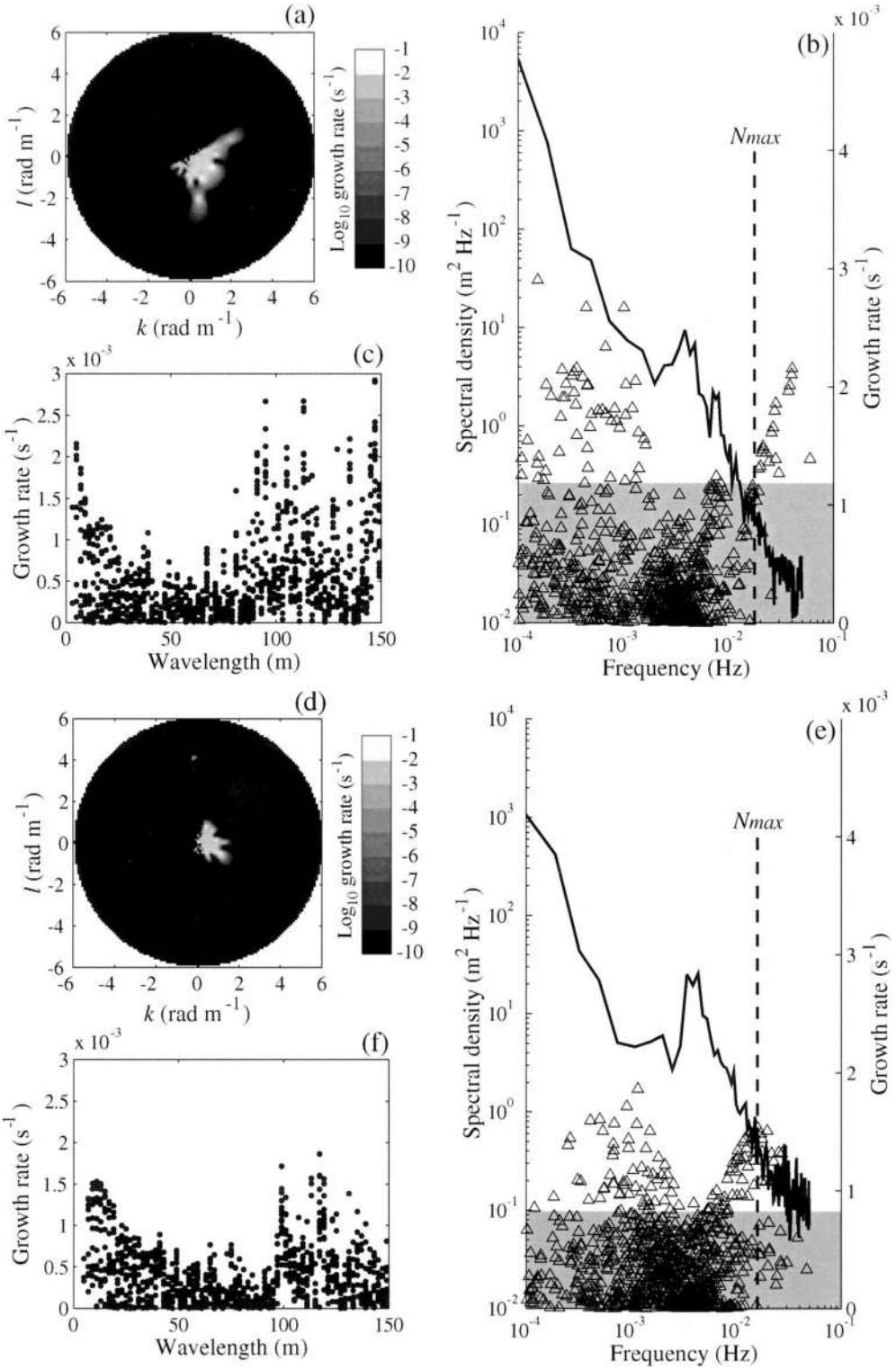

Fig. 17. Same as Fig. 16 except $K = 2 \times 10^{-4}$ m^2 s^{-1} at T1 and $K = 5 \times 10^{-4}$ m^2 s^{-1} at T2.

←

region where the growth period $1/\kappa c_i$ is greater than the average period Δt (shaded region), and the maximum N (dashed vertical line). The spectra were smoothed in the frequency domain to improve statistical confidence. Maximum growth rate of unstable modes versus wavelength at T1 (c) and T2 (f). Physical properties of the unstable modes are given in Table 2.

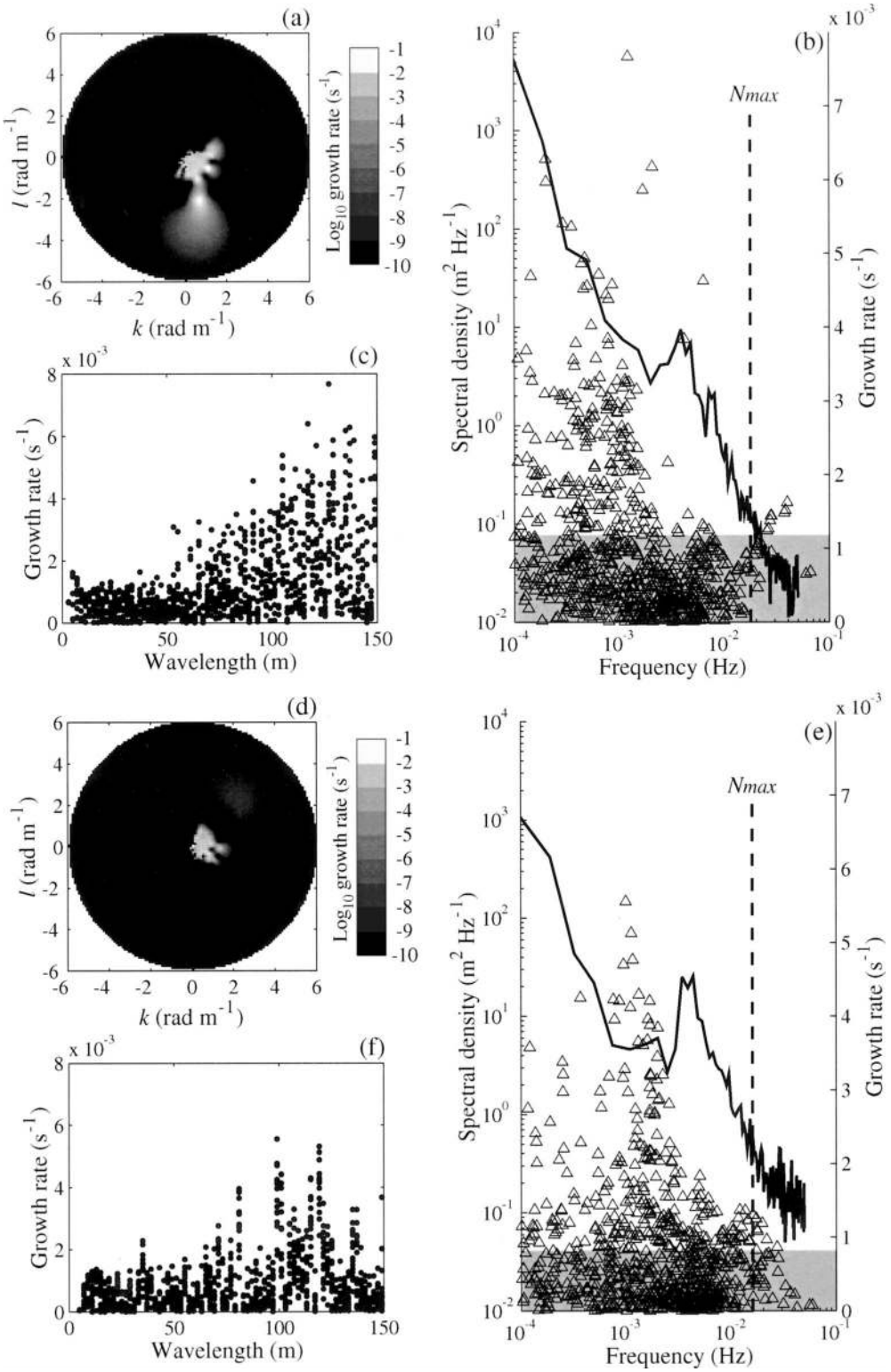

Fig. 18. Same as Fig. 16 except $K = 2 \times 10^{-4}$ m^2 s^{-1} at T1 and $K = 5 \times 10^{-3}$ m^2 s^{-1} at T2.

scale internal waves over the observed timescales of several days.

Conceptual models (e.g., Imberger 1998), laboratory experiments (e.g., Horn et al. 2001), and field observations (e.g., Gloor et al. 2000; Lemckert et al. pers. comm.) suggest that solitary and higher mode internal waves will propagate to the lake perimeter, where they will shoal on sloping boundaries and can lose up to 70% of their energy to the

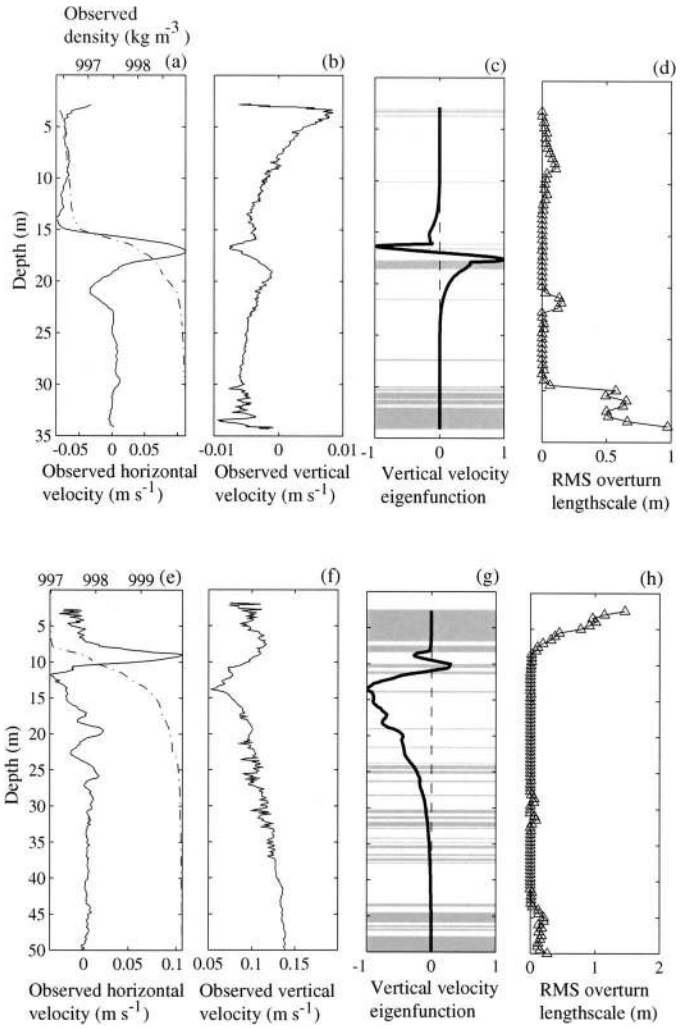

Fig. 19. Water column profiles from PFP casts and for most unstable modes in Fig. 15. Observed density (broken line) and horizontal velocity (solid line) at T3 (a) and BN50 (e). Observed vertical velocity at T3 (b) and BN50 (f). Vertical velocity eigenfunction $\hat{\psi}(z)$ for most unstable mode with $K = 0$ (solid line) and depths were Ri $<$ ¼ (shaded) at T3 (c) and BN50 (g). L_T is the RMS of 0.5-m binned displacements which has been required to monotonize the temperature profile which has been resampled as an average over 0.05-m intervals; L_T at T3 (d) and BN50 (h).

maintenance of the BBL (Michallet and Ivey 1999; Ivey et al. 2000). In addition to the shoaling of solitary and higher mode internal waves, contributions to dissipation in the BBL also arise from shear induced by basin-scale baroclinic currents. Although some models have shown that the shear-induced viscous component of BBL dissipation alone could account for this rapid decay of basin-scale internal waves (Fischer et al. 1979; Fricker and Nepf 2000; Gloor et al. 2000), observational evidence suggest that localized shoaling of solitary and higher mode internal waves might result in significant energy flux from the basin-scale wave field to dissipation and mixing within the BBL (e.g., Michallet and Ivey 1999). To determine whether the observed high-frequency internal waves can propagate to the lake boundary, we evaluated their characteristic horizontal decay length scales L_D.

For the high-frequency internal waves associated with shear instability, L_D was calculated as the maximum of $L_D = c_r/\kappa c_i$ (i.e., the waves continue to grow until their energy is dissipated through nonlinear billowing) and $L_D = c_r T_D$ (i.e., the waves propagate without billowing and are robbed of their energy by the ambient turbulence). From Fig. 23, $T_D > 1/\kappa c_i$ below the high-frequency spectral energy peak; therefore, for the most unstable modes at each wavelength beneath this peak, we calculate the maximum $L_D = c_r T_D \approx 637 \pm 425$ and 428 ± 219 m at T1 and T2, respectively. The mean radius of Lake Kinneret is ~10 km or 20 L_D, indicating that these waves will not reach the lake boundary. This result agrees with the theoretical arguments of LeBlond (1966) that linear internal waves with $\lambda \simeq 100$ m will be rapidly attenuated by ambient turbulence.

For the internal solitary waves believed to be excited by nonlinear process, we applied the simple self-induced shear model by Bogucki and Garrtett (1993). The energy within the three large vertical mode 1 internal solitary waves of depression shown in Fig. 12 was estimated by assuming an interface thickness of 5 m $< h <$ 10 m and using the data in Table 3. The critical amplitude $a_c \approx 2\sqrt{hh_1} \approx 15$–$22$ m is greater than the observed amplitude, $a \approx 11.4$ m, indicating that the internal solitary waves will not appreciably decay through self-induced interfacial shear as they propagate toward the lake boundary. Energy loss to turbulent eddies that are independent of and small in comparison to the wavelength was neglected (LeBlond 1966; Bogucki and Garrett 1993). For each wave, the total energy is estimated as $E_{tot} \approx (4/3)g'\rho_1 a^2 L \approx 1.6 \times 10^5$ J m^{-1}. Assuming the internal solitary wave width scales as the width of the Kelvin wave and using the volumetric average energy estimates of Imberger (1998) or Saggio and Imberger (1998) results in each internal solitary wave having ~1% of the basin-scale vertical mode 1 Kelvin wave energy. Although this value is quite low, consideration of the number of internal solitary waves in Fig. 8c suggests that, in lakes where internal solitary waves are observed (*see* Horn et al. 2001 and references therein), production and shoaling of these waves could be a significant energy flux path from the basin-scale wave field to the BBL.

The conceptual model suggested by these results can be described as follows. The basin-scale internal wave field, which is energized by surface wind forcing, can be decomposed into the coupled basin-scale baroclinic components of the horizontal velocity domain (currents) and the vertical velocity domain (waves). Degenerative nonlinear processes within the wave domain then erode the basin-scale wave energy through the production of solitons, which in turn propagate to the lake boundary where they can shoal and directly energize the BBL. The horizontal currents simultaneously erode the basin-scale wave energy through buoyancy flux and dissipation, which result from patchy shear instability within the lake interior and from the baroclinic currents that oscillate across the lake bed.

We have presented field observations that reveal ubiquitous and sometimes periodic high-frequency internal wave

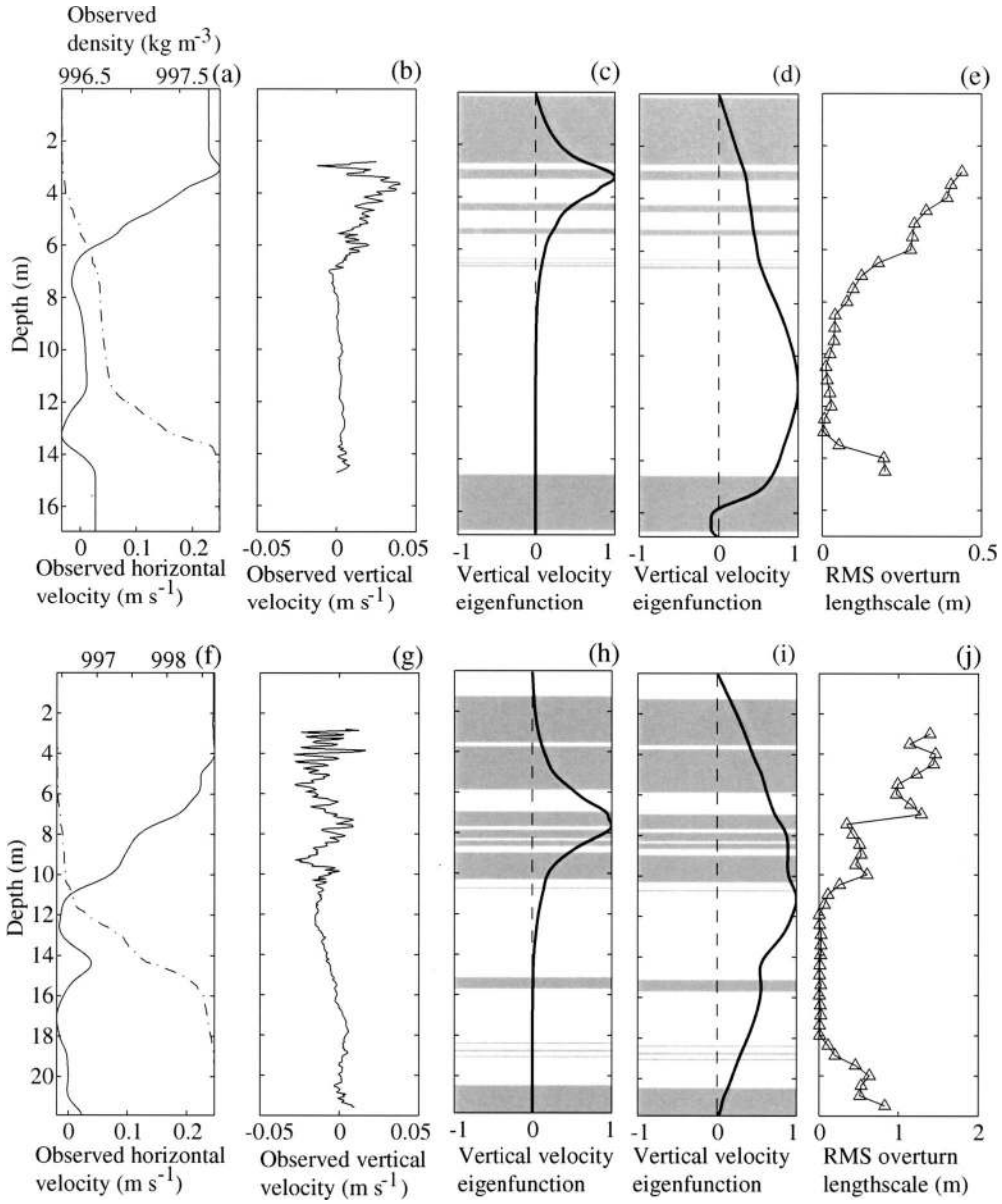

Fig. 20. Water column profiles from PFP casts and for most unstable modes in Fig. 16 and 18. Observed density (broken line) and horizontal velocity (solid line) at T1 (a) and T2 (f). Observed vertical velocity at T1 (b) and T2 (g). Vertical velocity eigenfunction $\hat{\psi}(z)$ for most unstable mode with $K = 0$ (solid line) and depths were Ri $<$ ¼ (shaded) at T1 (c) and T2 (h). Vertical velocity eigenfunction $\hat{\psi}(z)$ for most unstable mode with $K = 5 \times 10^{-1}$ at T1 (d) and $K = 10^{-3}$ at T2 (i) (solid lines) and depths were Ri $<$ ¼ (shaded). L_T is the RMS of 0.5-m binned displacements which has been required to monotonize the temperature profile, which has been resampled as an average over 0.05-m intervals; L_T at T1 (e) and T2 (j).

events within two large stratified lakes. Depending on the class of waves, the waves were found to be reasonably described by either liner stability or weakly nonlinear KdV models.

In regions of high shear and low Ri, two distinct classes of high-frequency internal waves were observed. Packets of relatively high-frequency and small-amplitude vertical mode 1 waves, vertically coherent in both phase and frequency, were typically observed riding on the crests of basin-scale Kelvin waves and during periods of intense surface wind forcing. These waves manifest a sharp spectral peak just below the local N near 10^{-2} Hz. Phase coherence observations and linear stability analysis suggest that these waves have wavelengths and phase velocities near 30–40 m and 15 cm s^{-1}, respectively. Irregular lower amplitude internal waves that vary vertically in frequency and phase were also observed in the region of high shear above and below the thermocline jets. These waves were accompanied by an abrupt

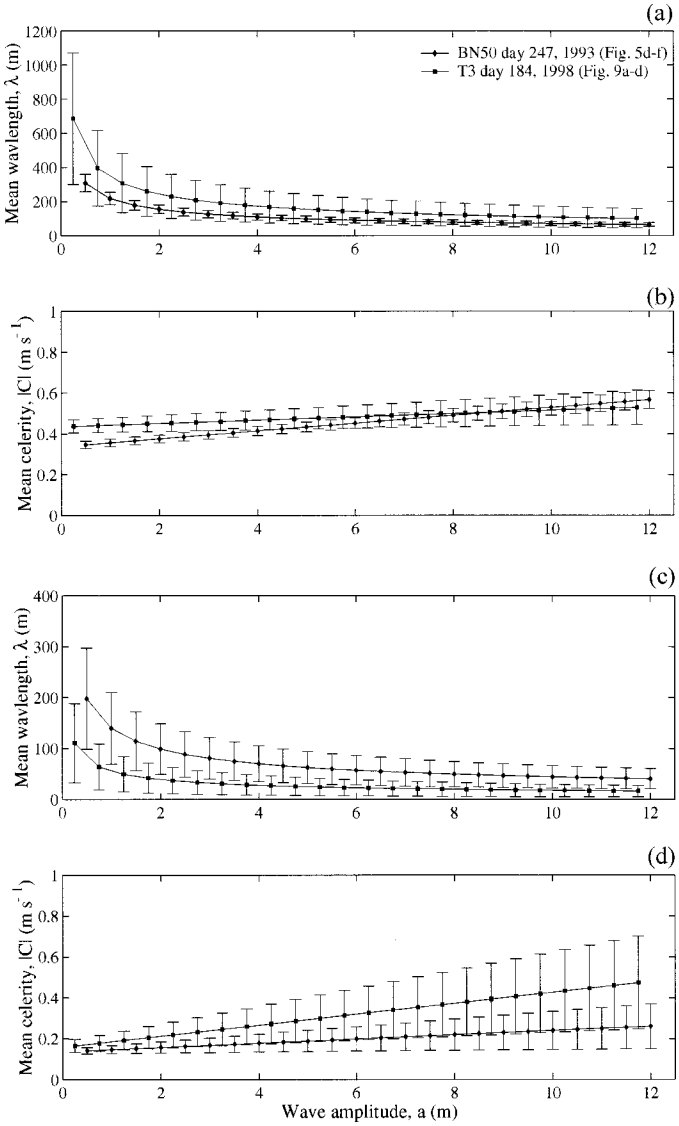

Fig. 21. Mean theoretical wavelength (3.6L) and mean nonlinear phase velocity of all stable modes over all azimuthal radii where κ and K are set to zero. Error bars denote standard deviation and are an indication of the theoretical influence of mean shear. Vertical mode 1 wavelength (a) and phase velocity (b) solutions versus soliton amplitude at T3 and BN50. Vertical mode 2 wavelength (c) and phase velocity (d) solutions versus soliton amplitude at T3 and BN50.

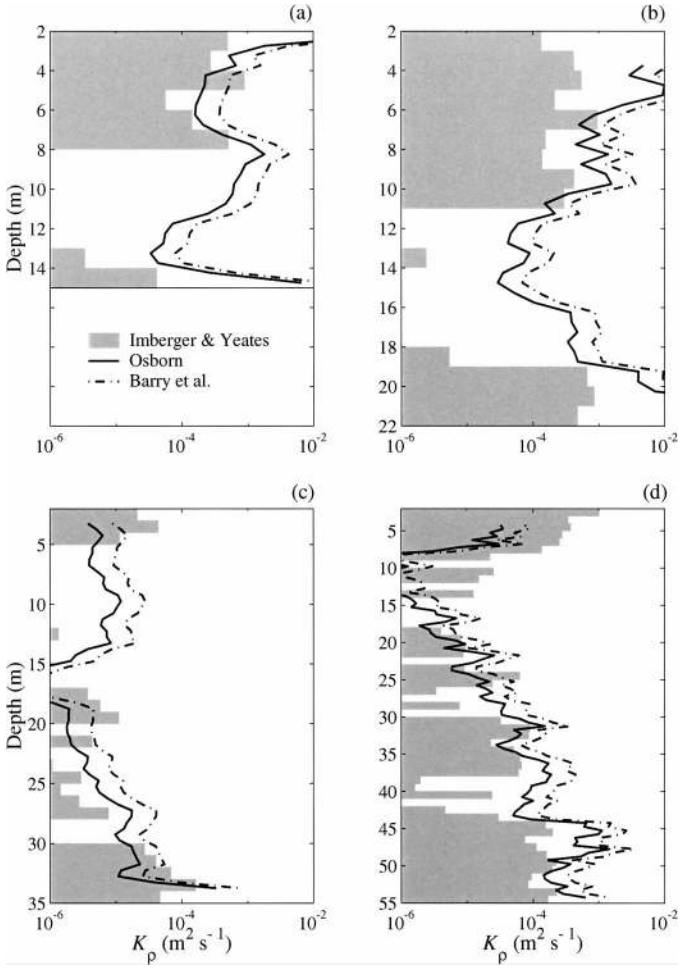

Fig. 22. Profiles of vertical eddy diffusivity (K_ρ) calculated using $K_\rho \leq 0.2(\varepsilon/N^2)$ (Osborn 1980), $K_\rho = 0.47(\varepsilon/N^2)$ (Barry et al. 2001), and $K_\rho = 3 \times 10^{-5}\mathrm{Ri}^{-0.5}$ for $\mathrm{Ri} \leq 0.1$ and $K_\rho = 9.3 \times 10^{-12}\mathrm{Ri}^{-7}$ for $\mathrm{Ri} > 0.1$ (Imberger and Yeates unpubl.). (a) T1, (b) T2, (c) T3, and (d) BN50. N and Ri profiles were determined from PFP casts used as input to the linear stability solver, and ε was estimated from the results of Saggio and Imberger (1998) to be 10^{-6} m^2 s^{-3} at T1 and T2 and 10^{-8} m^{-2} s^3 at T3 and BN50. These estimates of ε are representative of the base of the epilimnion and through the metalimnion and are thus strictly invalid at other depths.

thickening of the metalimnion and manifest a broader spectral peak near 10^{-2} Hz. Phase coherence observations and linear stability analysis suggest that these waves have wavelengths and phase velocities near 10–35 m and 5–15 cm s^{-1}, respectively.

Large-amplitude vertical mode 1 and mode 2 internal solitons were observed near discontinuous density fronts associated with basin-scale wave forcing. These waves excite a broad spectral peak near 10^{-3} Hz. Direct observation and results from analytical models suggest that the vertical mode 1 solitons have wavelengths of several hundred meters and phase velocities near 100 cm s^{-1}, whereas the vertical mode 2 solitons have wavelengths of several tens of meters and phase velocities between 20 and 50 cm s^{-1}. The mode 1 solitons were found to each contain ~1% of the energy within the basin-scale internal wave field.

The waves associated with shear instability were shown to dissipate their energy within the lake interior, thus possibly accounting for sporadic elevated observation of ε within the metalimnion (Saggio and Imberger 2001). Conversely, the nonlinear waves were found to be capable of propagating to the lake perimeter where they can shoal, thus releasing their energy directly to the benthic boundary layer via turbulent mixing and dissipation.

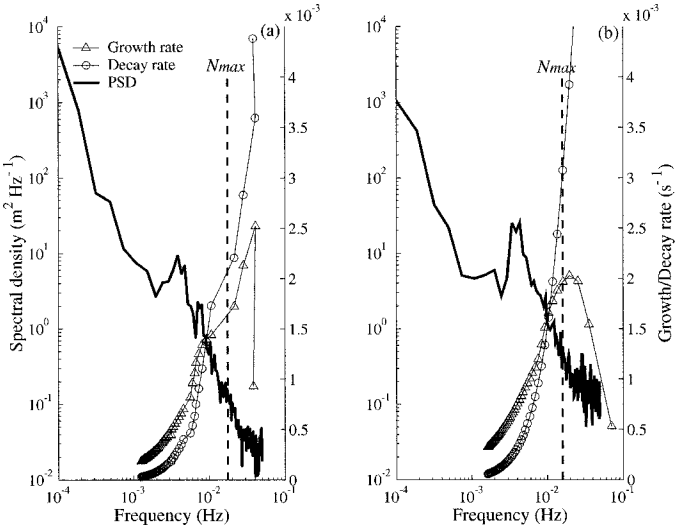

Fig. 23. Maximum growth rate (κc_i) and decay rate ($1/T_D$) of the most unstable mode at each wavelength at T1 (a) and T2 (b) with $K = 0$. Decay rate variables $\varepsilon \approx 10^{-6}$ m^2 s^{-3}, $H = 6$ m, and $w_o = 0.04$ m s^{-1} and 0.03 m s^{-1} at T1 and T2, respectively. Also plotted are the 27°C isotherm displacement spectra as observed from a moored thermistor chain at each location (solid line) and the maximum N (dashed vertical line). The spectra were smoothed in the frequency domain to improve statistical confidence.

References

ANTENUCCI, J. P., AND J. IMBERGER. 2001. On internal waves near the high frequency limit in an enclosed basin. J. Geophys. Res. **106:** 22,465–22,472.

———, ———, AND A. SAGGIO. 2000. Seasonal evolution of the basin-scale internal wave field in a large stratified lake. Limnol. Oceanogr. **45:** 1621–1638.

APEL, J. R., J. R. HOLBROOK, A. K. LIU, AND J. J. TSAI. 1985. The Sulu Sea internal soliton experiment. J. Phys. Oceanogr. **15:** 1625–1650.

BARRY, M. E., G. N. IVEY, K. B. WINTERS, AND J. IMBERGER. 2001. Measurements of diapycnal diffusivities in stratified fluids. J. Fluid Mech. **442:** 267–291.

BATCHELOR, G. K. 1967. An introduction to fluid dynamics. Cambridge Univ. Press.

BENNY, D. J. 1966. Long nonlinear waves in fluid flows. J. Math. Phys. **45:** 52–63.

BOGUCKI, D., AND C. GARRETT. 1993. A simple model for the shear-induced decay of an internal solitary wave. J. Phys. Oceanogr. **23:** 1767–1776.

DESAUBIES, Y. J. F. 1975. A linear theory of internal wave spectra and coherences near the Väisälä frequency. J. Geophys. Res. **80:** 895–899.

ECKART, C. 1960. Hydrodynamics of oceans and atmospheres. Pergamon.

FARMER, D. M. 1978. Observations of long nonlinear internal waves in a lake. J. Phys. Oceanogr. **8:** 63–73.

———, AND L. ARMI. 1999. The generation and trapping of internal solitary waves over topography. Science **283:** 188–190.

FISCHER, H. B., E. J. LIST, R. C. Y. KOH, J. IMBERGER, AND N. H. BROOKS. 1979. Mixing in inland and coastal waters. Academic.

FRICKER, P. D., AND H. M. NEPF. 2000. Buoyancy effects and internal seiche decay, p. 313–318. *In* G. A. Lawrence, R. Pieters, and N. Yonemitsu [eds.], Proceedings of the Fifth International Symposium on Stratified Flow, Vancouver, British Columbia. Dept. Civil Eng., Univ. British Columbia.

GARRETT, C. , AND W. MUNK. 1975. Space–time scales of internal waves: A progress report. J. Geophys. Res. **80:** 291–297.

———, AND ———. 1979. Internal waves in the ocean. Ann. Rev. Fluid Mech. **11:** 339–369.

GILL, A. E. 1982. *Atmosphere–ocean dynamics.* Academic.

GLOOR, M., A. WÜEST, AND D. M. IMBODEN. 2000. Dynamics of mixed bottom boundary layers and its implications for diapycnal transport in a stratified, natural water basin. J. Geophys. Res. **105:** 8629–8646.

GOUDSMIT, G.-H., F. PETERS, GLOOR, M. AND A. WÜEST. 1997. Boundary versus internal diapycnal mixing in stratified natural waters. J. Geophys. Res. **102:** 27,903–27,914.

GREGG, M. C. 1987. Diapycnal mixing in the thermocline: A review. J. Geophys. Res. **92:** 5249–5286.

GROEN, P. 1948. Contribution to the theory of internal waves. Koninkl. Ned. Meteorol. Inst., Medd. Verh. **125:** 1–23.

HAMBLIN, P. F. 1977. Short-period internal waves in the vicinity of a river-induced shear zone in a fjord lake. J. Geophys. Res. **82:** 3167–3174.

HOGG, A. M., K. B. WINTERS, AND G. N. IVEY. 2001. Linear internal waves and the control of stratified exchange flows. J. Fluid Mech. **447:** 357–375.

HOLLOWAY, P. E. 1987. Internal hydraulic jumps and solitons at a shelf break region on the Australian North West Shelf. J. Geophys. Res. **92:** 5405–5416.

HOLMBOE, J. 1962. On the behaviour of symmetric waves in stratified shear layers. Geofys. Publ. **24:** 67–113.

HORN, D. A., J. IMBERGER AND G. N. IVEY. 2001. The degeneration of large-scale interfacial gravity waves in lakes. J. Fluid Mech. **434:** 181–207.

HUNKINS, K., AND M. FLIEGEL. 1973. Internal undular surges in Seneca Lake: A natural occurrence of solitons. J. Geophys. Res. **78:** 539–548.

IMBERGER, J. 1998. Flux paths in a stratified lake: A review, p. 1–18. *In* J. Imberger [ed.]., Physical processes in lakes and oceans. Coastal and estaurine studies, 54, American Geophysical Union.

IVEY, G. N., AND J. IMBERGER. 1991. On the nature of turbulence in a stratified fluid. Part 1: The energetics of mixing. J. Phys. Oceanogr. **21:** 650–658.

———, K. B. WINTERS, AND I. P. D. DE SILVA. 2000. Turbulent mixing in a sloping benthic boundary layer energized by internal waves. J. Fluid Mech. **418:** 59–76.

KOPPEL, D. 1964. On the stability of thermally stratified fluid under the action of gravity. J. Math. Phys. **5:** 963–982.

LAWRENCE, G. A., S. P. HAIGH, AND Z. ZHU. 1998. In search of Holmboes instability, p. 295–304. *In* J. Imberger [ed.] *Physical processes in lakes and oceans.* Coastal and estaurine studies, v. 54, AGU.

LEBLOND, P. H. 1966. On the damping of internal gravity waves in a continuously stratified ocean. J. Fluid Mechn. **25:** 121–142.

LEDWELL, J. R., E. T. MONTGOMERY, K. L. PLOZIN, L. C. S. LAURENT, R. W. SCHMITT, AND J. M. TOOLE. 2000. Evidence for enhanced mixing over rough topography in the abyssal ocean. Nature **403:** 179–182.

LEDWELL, J. R., A. J. WATSON, AND C. S. LAW. 1993. Evidence for slow mixing across the pycnocline from an open-ocean tracer-release experiment. Nature **364:** 701–703.

MAXWORTHY, T., J. IMBERGER, AND A. SAGGIO. 1998. A laboratory demonstration of a mechanism for the production of secondary, internal gravity-waves in a stratified fluid, p. 261–270. *In* J. Imberger [ed.], Physical processes in lakes and oceans. Coastal and estaurine studies, v. 54, American Geophysical Union.

MICHALLET, H., AND G. N. IVEY. 1999. Experiments on mixing due

to internal solitary waves breaking on uniform slopes. J. Geophys. Res. **104:** 13,467–13,477.

MORTIMER, C. H. 1987. Fifty years of physical investigations and related limnological studies on Lake Erie, 1928–1977. J. Great Lakes Res. **13:** 407–435.

———, AND W. HORN. 1982. Internal wave dynamics and their implications for plankton biology in the Lake of Zurich. Mitt. Int. Ver. Limnol. 127: 299-318.

———, D. C. MCNAUGHT, AND K. M. STEWART. 1968. Short internal waves near their high-frequency limit in central Lake Michigan, p. 454–469. *In* Proceedings of the 11th Conference on Lakes Research. Int. Assoc. Great Lakes Res.

MUNK, W. H. 1966. Abyssal recipies. Deep-Sea Res. **13:** 707–370.

NISHIDA, S., AND S. YOSHIDA. 1987. Stability and eigenfunctions of disturbances in stratified two-layer shear flows. *In* Proceedings of the Third Internal Symposium on Stratified Flow, Pasadena, California.

OSBORN, T. R. 1980. Estimates of the local rate of vertical diffusion from dissipation measurements. J. Phys. Oceanogr. **10:** 89–89.

POLZIN, K. L., J. M. TOOLE, J. R. LEDWELL, AND F. W. SCHMITT. 1997. Spatial variability of turbulent mixing in the abyssal ocean. Science **276:** 93–96.

SAGGIO, A., AND J. IMBERGER. 1998. Internal wave weather in stratified lakes. Limnol. Oceanogr. **43:** 1780–1795.

———, AND ———. 2001. Mixing and turbulent fluxes in the metalimnion of a stratified lake. Limnol. Oceanogr. **46:** 392–409.

SCHMIDT, N. P., AND R. H. SPIGEL. 2000. Second mode internal solitary waves I: Integral properties. *In* Proceedings of the Fifth International Symposium on Stratified Flow, Vancouver, British Columbia.

SMYTH, W. D., AND W. R. PELTIER. 1990. Three-dimensional primary instabilities of a stratified, dissipative, parallel flow. Geophys. Astrophys. Fluid Dyn. **52:** 249–261.

———, AND ———. 1994. three-dimensionalization of barotropic vortices on the *f*-plane. J. Fluid Mech. **265:** 25–64.

———, G. P. KLASSEN, AND W. R. PELTIER. 1988. Finite amplitude Holmboe waves. Geophys. Astrophys. Fluid Dyn. **43:** 181–222.

SUN, C., W. D. SMYTH, AND J. N. MOUM. 1998. Dynamic instability of stratified shear flow in the upper equatorial pacific. J. Geophys. Res. **103:** 10,323–10,337.

THORPE, S. A. 1978. The near-surface ocean mixing layer in stable heating conditions. J. Geophys. Res. **83:** 2875–2885.

———. 1998. Some dynamical effects of internal waves and the sloping sides of lakes, p. 441–460. *In* J. Imberger [ed.], Physical processes in lakes and oceans. Coastal and Estaurine Studies, v. 54, AGU.

———, J. M. KEEN, R. JIANG, AND U. LEMMIN. 1996. High-frequency internal waves in Lake Geneva. Philos. Trans. R. Soc. Lond, A **354:** 237–257.

TURNER, J. S. 1973. Buoyancy effects in fluids. Cambridge Univ. Press.

WOODS, J. D. 1968. Wave-induced shear instability in the summer thermocline. J. Fluid Mech. **32:** 791–800.

WÜEST, A., G. PIEPKE, AND D. C. SENDEN. 2000. Turbulent kinetic energy balance as a tool for estimating vertical diffusivity in wind-forced stratified waters. Limnol. Oceanogr. **45:** 1388–1400.

Received: 7 February 2001
Accepted: 1 October 2002
Amended: 22 October 2002